

THE MOST LUMINOUS GALAXIES DISCOVERED BY WISE

CHAO-WEI TSAI^{1,2}, PETER R. M. EISENHARDT¹, JINGWEN WU³, DANIEL STERN¹, ROBERTO J. ASSEF⁴,
ANDREW W. BLAIN⁵, CARRIE R. BRIDGE⁶, DOMINIC J. BENFORD⁷, ROC M. CUTRI⁸, ROGER L. GRIFFITH⁹, THOMAS H.
JARRETT¹⁰, CAROL J. LONSDALE¹¹, FRANK J. MASCI⁸, LEONIDAS A. MOUSTAKAS¹, SARA M. PETTY¹², JACK SAYERS⁶, S.
ADAM STANFORD¹³, EDWARD L. WRIGHT³, LIN YAN⁸, DAVID T. LEISAWITZ⁷, FENGCHUAN LIU¹, AMY K. MAINZER¹, IAN S.
MCLEAN³, DEBORAH L. PADGETT⁷, MICHAEL F. SKRUTSKIE¹⁴, CHRISTOPHER R. GELINO⁸, CHARLES A. BEICHMAN⁸,
STÉPHANIE JUNEAU¹⁵

The Astrophysical Journal, in Press

ABSTRACT

We present 20 *Wide-field Infrared Survey Explorer* (*WISE*)-selected galaxies with bolometric luminosities $L_{\text{bol}} > 10^{14} L_{\odot}$, including five with infrared luminosities $L_{\text{IR}} \equiv L_{(\text{rest } 8-1000 \mu\text{m})} > 10^{14} L_{\odot}$. These “extremely luminous infrared galaxies,” or ELIRGs, were discovered using the “W1W2-dropout” selection criteria (Eisenhardt et al. 2012) which requires marginal or non-detections at 3.4 and 4.6 μm (*W1* and *W2*, respectively) but strong detections at 12 and 22 μm in the *WISE* survey. Their spectral energy distributions are dominated by emission at rest-frame 4–10 μm , suggesting that hot dust with $T_d \sim 450 \text{ K}$ is responsible for the high luminosities. These galaxies are likely powered by highly obscured active galactic nuclei (AGNs), and there is no evidence suggesting these systems are beamed or lensed. We compare this *WISE*-selected sample with 116 optically selected quasars that reach the same L_{bol} level, corresponding to the most luminous unobscured quasars in the literature. We find that the rest-frame 5.8 and 7.8 μm luminosities of the *WISE*-selected ELIRGs can be 30–80% higher than that of the unobscured quasars. The existence of AGNs with $L_{\text{bol}} > 10^{14} L_{\odot}$ at $z > 3$ suggests that these supermassive black holes are born with large mass, or have very rapid mass assembly. For black hole seed masses $\sim 10^3 M_{\odot}$, either sustained super-Eddington accretion is needed, or the radiative efficiency must be $< 15\%$, implying a black hole with slow spin, possibly due to chaotic accretion.

Subject headings: infrared: galaxies; galaxies: active; quasars: supermassive black holes

1. INTRODUCTION

Hyperluminous infrared galaxies (Cutri et al. 1994), or HyLIRGs, are galaxies whose infrared luminosity (L_{IR}) exceeds $10^{13} L_{\odot}$ (Sanders & Mirabel 1996). They have

¹ Jet Propulsion Laboratory, California Institute of Technology, 4800 Oak Grove Dr., Pasadena, CA 91109, USA

² NASA Postdoctoral Program Fellow; [email: Chao-Wei.Tsai@jpl.nasa.gov]

³ Department of Physics and Astronomy, UCLA, Los Angeles, CA 90095-1547

⁴ Núcleo de Astronomía de la Facultad de Ingeniería, Universidad Diego Portales, Av. Ejército Libertador 441, Santiago, Chile.

⁵ Department of Physics & Astronomy, University of Leicester, 1 University Road, Leicester, LE1 7RH, UK

⁶ Division of Physics, Math, and Astronomy, California Institute of Technology, Pasadena, CA 91125, USA

⁷ NASA Goddard Space Flight Center, Greenbelt, MD 20771, USA

⁸ Infrared Processing and Analysis Center, California Institute of Technology, Pasadena, CA 91125, USA

⁹ Department of Astronomy and Astrophysics, The Pennsylvania State University, 525 Davey Lab, University Park, PA 16802, USA

¹⁰ Astronomy Department, University of Cape Town, Private Bag X3, Rondebosch 7701, South Africa

¹¹ National Radio Astronomy Observatory, 520 Edgemont Road, Charlottesville, VA 22903, USA

¹² Department of Physics, Virginia Tech, Blacksburg, VA, 24061, USA

¹³ Department of Physics, University of California Davis, One Shields Avenue, Davis, CA 95616, USA

¹⁴ Department of Astronomy, University of Virginia, Charlottesville, VA 22903, USA

¹⁵ CEA-Saclay, DSM/IRFU/SAP, F-91191 Gif-sur-Yvette, France

generally been discovered due to their substantial IR emission from far-IR surveys such as those with the *Infrared Astronomical Satellite* (*IRAS*), (Neugebauer et al. 1984), the Submillimetre Common-User Bolometer Array (SCUBA) at James Clerk Maxwell Telescope, or, more recently, the *Herschel Space Telescope* (Cutri et al. 1994; Frayer et al. 1998; Rowan-Robinson 2000, and references therein; Casey et al. 2012b). Infrared emission dominates the energy output of these hyperluminous systems, so their L_{IR} is approximately equal to their bolometric luminosity L_{bol} . Galaxies with such high luminosity, usually powered by AGN (Weedman et al. 2012), intense starbursts (Rowan-Robinson 2000), or a mixture of both, represent a rapid growth phase of the supermassive black holes (SMBHs) and/or the stellar mass portfolio of the host galaxies. It has been suggested that this phase at $1 < z < 3$ dominates both the stellar mass assembly of massive galaxies and the mass accretion of SMBHs (Hopkins et al. 2006a, 2008).

Both observations and simulations suggest that the high accretion rate phase of AGNs occurs after the major merging event of two large galaxies (Sanders et al. 1988; Hopkins et al. 2008). At that stage, gas from the two parent galaxies loses angular momentum due to cloud–cloud collisions, quickly sinks to the center of the coalescing galaxy, and fuels the AGN which is still shrouded by a dusty cocoon. As the AGN accretes, its luminosity increases dramatically, and it becomes a quasar. At early stages of AGN accretion, the infalling dust and gas may cause severe obscuration toward the quasar, making it difficult to identify at optical wavelengths. The

intense starburst induced by the gas cloud collisions is quickly followed by an optically luminous quasar phase, and eventually suppressed by feedback from the quasar (Silk & Rees 1998; Springel et al. 2005).

Some optical quasars have comparable intrinsic L_{bol} to the extreme luminosity end of the HyLIRG population ($> 10^{14} L_{\odot}$), such as S5 0014+81 (Osmer et al. 1994), SDSS J1701+6412 (Hewett & Wild 2010), and HS 1946+7658 (Lu et al. 1996). These quasars have SMBH masses of $\sim \text{few} \times 10^9 M_{\odot}$ or higher, if they are emitting at or close to the Eddington limit. At the Eddington limit, SMBH mass grows on the Salpeter e -folding time scale of 45 Myr (Salpeter 1964), and the most massive SMBHs can reach $\sim 3 \times 10^{10} M_{\odot}$ at $z > 2$ (Kelly et al. 2010) in the broad-line QSO phase. The discovery of hyper-luminous quasars at $z > 6$ (Fan et al. 2001) further suggests that SMBHs can grow to $10^9 M_{\odot}$ (Barth et al. 2003; Willott et al. 2005; Mortlock et al. 2011) by the time the universe is only ~ 1 Gyr old. The existence of such luminous quasars at early times constrains SMBH seed masses and their growth history (Volonteri & Rees 2006), implying a high accretion rate at high redshift, rather than slower accretion over a Hubble time (Hopkins et al. 2006b).

By selection, optical quasars have relatively low extinction at visible wavelengths, suggesting that feedback to the ambient material may have cleared out the surrounding dust cocoon and terminated further accretion or star formation in the inner regions of the host galaxy. Several lines of evidence suggest that quasars must have spent significant time growing in the obscured phase (Kelly et al. 2010; Assef et al. 2015), and the 20–30 keV peak of the cosmic X-ray background implies that most black hole growth is obscured (Gilli et al. 2007). Key open questions for understanding quasar evolution include: What was the SMBH activity just prior to the quasar “blowout” phase, when the SMBH was still highly embedded in dust and gas from the parent galaxy coalescence event? Were the SMBHs accreting as rapidly as optical quasars, faster than quasars because of the infalling material, or was the accretion suppressed by the dynamical interaction? Answers to these questions may be hidden in highly obscured, but still powerful quasars.

The *Wide-field Infrared Survey Explorer* (*WISE*), which surveyed the entire sky at 3.4, 4.6, 12, and 22 μm , was designed to identify nearby cool brown dwarfs and the most luminous dusty galaxies in the universe (Wright et al. 2010). By selecting objects with marginal or no detection in the *WISE* 3.4 and 4.6 μm bands and strong detections in the 12 and 22 μm bands, we have discovered a population of hyperluminous galaxies with $L_{\text{bol}} > 10^{13} L_{\odot}$ (Eisenhardt et al. 2012; Wu et al. 2012; Bridge et al. 2013). Spectroscopy reveals that these “W1W2-dropouts” are predominantly systems at redshift $1.6 < z < 4.6$ (Assef et al. 2015; P. R. M. Eisenhardt et al. in preparation). Extended Ly α emission is observed in a large fraction of these systems, and may be the result of strong AGN feedback (Bridge et al. 2013). Their steeply rising spectral energy distributions (SEDs) from rest frame 1–10 μm and decreasing luminosity contribution at longer wavelengths imply that the bulk of the energy in these galaxies is radiated by hot dust (Wu et al. 2012). They meet the selection crite-

ria for dust-obscured galaxies (DOGs; $F_{24 \mu\text{m}} > 0.3 \text{ mJy}$ and $F_{24 \mu\text{m}}/F_R > 1000$; Dey et al. 2008), but have hotter dust temperatures ($> 60 \text{ K}$; Wu et al. 2012; Bridge et al. 2013; Jones et al. 2014) than DOGs (30K–40K; Pope et al. 2008; Melbourne et al. 2012). Thus, we also refer to this population as “Hot DOGs” (Wu et al. 2012).

Here we examine the most luminous Hot DOGs identified, corresponding to galaxies with $L_{\text{bol}} > 10^{14} L_{\odot}$. Luminosities this high correspond to a star formation rate of many thousands of solar masses per year, or to a SMBH accretion rate of tens of solar masses per year. If this luminosity is maintained for $\sim 10^8$ yrs, these high luminosity sources represent the main growth phase for stellar mass if they are powered by starbursts, or of SMBH mass if they are powered by AGNs. From spectroscopic and far-infrared followup observations of over 200 Hot DOGs we have identified 20 that meet this L_{bol} threshold. Among these 20 Hot DOGs five have intrinsic $L_{\text{IR}} \equiv L_{(\text{rest } 8-1000 \mu\text{m})} > 10^{14} L_{\odot}$, an order magnitude higher than the HyLIRG luminosity threshold. We refer to such systems as “extremely luminous infrared galaxies,” or ELIRGs. The rest of our sample has $L_{\text{IR}} > 5 \times 10^{13} L_{\odot}$, which should be considered a conservative lower limit due to our luminosity estimate approach (see § 3.3). For convenience, we refer to these slightly less luminous objects as ELIRGs as well throughout this paper. For comparison, we also present 116 optically selected quasars from the literature with $L_{\text{bol}} > 10^{14} L_{\odot}$.

We present the sample and mid-IR and far-IR observations in Section 2. Our luminosity estimates are detailed in Section 3. The implications of the high luminosities are discussed in Section 4, followed by a summary in Section 5. We adopt a cosmology with $H_0 = 70 \text{ km s}^{-1} \text{ Mpc}^{-1}$, $\Omega_m = 0.3$, and $\Omega_{\Lambda} = 0.7$.

2. SAMPLE AND OBSERVATIONS

The *WISE* ELIRGs presented in this paper are from the subset of Hot DOGs selected from the *WISE* All-Sky Source Catalog (Cutri et al. 2012) with spectroscopic redshifts (P. R. M. Eisenhardt et al. in preparation) and far-infrared photometry. The redshift and L_{bol} distribution of the current Hot DOG sample is shown in Figure 1. The sample of 20 Hot DOGs with $L_{\text{bol}} \geq 10^{14} L_{\odot}$ corresponds to approximately 15% of the current sample with spectroscopic redshifts and multi-wavelength followup observations. The coordinates and redshifts of the 20 sources are listed in Table 1. The redshift quality flag “A” in Table 1 indicates unambiguous redshift typically determined from multiple emission or absorption features. The flag “B” signifies a less secure redshift determined from a robustly detected line but with uncertain identification of the line (Stern et al. 2002). The typical uncertainty in the redshift in Table 1 is $\Delta z \sim 0.002$.

The photometric measurements used in this paper are listed in Table 2. We include measurements of optical r' -band and selected near-IR bands from ground-based follow-up observations, mid-IR photometry from *WISE* and the *Spitzer Space Telescope*, and far-IR photometry from the *Herschel Space Telescope*¹⁶.

¹⁶ *Herschel* is an ESA space observatory with science instruments provided by European-led Principal Investigator consortia and with important participation from NASA.

Table 1
Properties of *WISE* ELIRGs

Source	<i>WISE</i> Coordinates		z	Q_z
	R.A. (J2000)	Decl. (J2000)		
W0116–0505	01:16:01.42	–05:05:04.2	3.173 ^a	A
W0126–0529	01:26:11.96	–05:29:09.6	2.937	B
W0134–2922	01:34:35.71	–29:22:45.4	3.047	A
W0149+2350	01:49:46.18	+23:50:14.6	3.228	A
W0220+0137	02:20:52.13	+01:37:11.4	3.122 ^a	A
W0255+3345	02:55:34.90	+33:45:57.8	2.668	A
W0410–0913	04:10:10.61	–09:13:05.2	3.592 ^a	A
W0533–3401	05:33:58.44	–34:01:34.5	2.904	A
W0615–5716	06:15:11.07	–57:16:14.6	3.399	B
W0831+0140	08:31:53.26	+01:40:10.8	3.888	A
W0859+4823	08:59:29.93	+48:23:02.0	3.245 ^a	A
W1248–2154	12:48:15.21	–21:54:20.4	3.318	A
W1322–0328	13:22:32.57	–03:28:42.2	3.043	A
W1838+3429	18:38:09.16	+34:29:25.9	3.205	B
W2042–3245	20:42:49.28	–32:45:17.9	3.963	B
W2201+0226	22:01:23.39	+02:26:21.8	2.877	A
W2210–3507	22:10:11.87	–35:07:20.0	2.814	B
W2246–0526	22:46:07.57	–05:26:35.0	4.593	A
W2246–7143	22:46:12.07	–71:44:01.3	3.458	A
W2305–0039	23:05:25.88	–00:39:25.7	3.106	A

Note. — The *WISE* coordinates are from the AllWISE database. The “ Q_z ” flag indicates the quality of the redshift (see Section 2 for details).

^a Redshift from Wu et al. (2012)

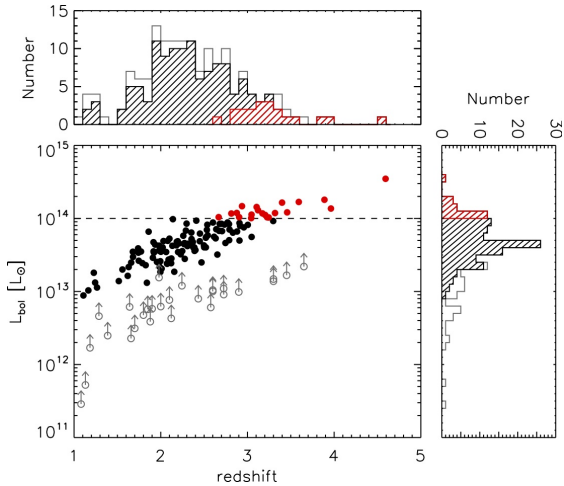


Figure 1. The redshift and bolometric luminosity, L_{bol} , of *WISE* Hot DOGs at $1 < z < 5$. The luminosity distribution of the confirmed Hot DOGs is on the right, and the redshift distribution is on the top. The black dots and black shaded regions represent Hot DOGs with *Herschel* measurements, while the gray open circles and open histograms indicate the lower luminosity limits for Hot DOGs without far-IR data. The red points and histogram are for the sample of objects presented in this paper which exceed the $L_{\text{bol}} > 10^{14} L_{\odot}$ threshold, shown by the horizontal dashed line.

2.1. Mid-infrared Observations

The mid-IR photometry of the *WISE* ELIRGs is listed in Table 2. *WISE* photometry is from the AllWISE Data Release (Cutri et al. 2013), which contains enhanced data products relative to the *WISE* All-Sky Source Catalog (Cutri et al. 2012) from improved data processing pipelines on the full 7 months of cryogenic data at 12 and 22 μm , and 12 months of both cryogenic and post-cryogenic data at 3.4 and 4.6 μm . By selection, the Hot DOGs are not well detected at *WISE* 3.4 and 4.6 μm in the 7-month *WISE* All-Sky Source Catalog. However,

more than half of them are detected at $\gtrsim 5\sigma$ using the deeper 3.4 and 4.6 μm data in the AllWISE Source Catalog. The [3.6] and [4.5] photometry for the *W1W2*-non-detected sources are from *Spitzer* IRAC obtained during the *Spitzer* warm mission phase, as reported by Griffith et al. (2012). For sources with AllWISE [3.4] and [4.6] detections, we convert the data to IRAC [3.6] and [4.5] using the color correction [3.6] = $W1 - 0.29 \times (W1 - W2)$ ¹⁷. The anticipated color difference in between IRAC [4.5] and *WISE* [4.6] is less than 0.1 magnitude¹⁷, or about 10% in flux density, thus no color correction has been applied for that band.

2.2. Far-IR and Submillimeter Observations

The far-IR and submillimeter photometry of the *WISE* selected ELIRGs, listed in Table 2, was acquired with *Herschel*. The *Herschel* data (PI: P. Eisenhardt, Proposal ID: OT1_peisenha_1 and OT2_peisenha_2) include both PACS (Poglitsch et al. 2010) and SPIRE (Griffin et al. 2010) observations. The SPIRE maps were made using small jiggle map mode, with a total 487 s integration time per source. The PACS images were obtained with two concatenated mini-scans for a total of 679 s on each source. The data were processed and analyzed with HIPE v11.1.0. For W0831+0140, which was not included in the *Herschel* program but was covered by the *Herschel* ATLAS survey (Eales et al. 2010), the far-IR photometry was taken from the public *Herschel* archive.

2.3. Extremely Luminous Optically Selected Quasars from the Literature

As a comparison sample, we identified known quasars with $L_{\text{bol}} > 10^{14} L_{\odot}$ from the following large-scale quasar catalogs: (i) the 13th edition of the Catalogue of Quasars and Active Nuclei (Véron-Cetty & Véron 2010), (ii) the 2dF QSO Redshift Survey (Croom et al. 2004), (iii) the 2dF-SDSS LRG and QSO Survey (Croom et al. 2009), (iv) the Sloan Digital Sky Survey (SDSS) Quasar Catalog V from the 7th SDSS data release (Schneider et al. 2010), and (v) the Sloan Digital Sky Survey Quasar Catalog from SDSS 9th data release (Pâris et al. 2012). In addition, we considered objects with the spectroscopic class of “QSO” in the SDSS 10th Data Release (DR10; Ahn et al. 2013). For the luminous SDSS DR10 quasar sample, we visually checked for mis-identified spectral features or artifacts. We also included 46 objects that are listed as “HyLIRGs” in the NASA/IPAC Extragalactic Database (2013 August 27th version). We utilized the redshift information of quasars reported in these catalogs, and estimated their bolometric luminosities using photometric data from *GALEX* GR7 (Martin et al. 2005), SuperCosmos (Hambly et al. 2001), SDSS DR10 (Ahn et al. 2013), 2MASS (Skrutskie et al. 2006), UKIDSS DR9 (Lawrence et al. 2007), the AllWISE Data Release (Cutri et al. 2013), *IRAS* (Neugebauer et al. 1984) and *Akari* (Murakami et al. 2007).

We then visually inspected the SEDs and images of ~ 1300 sources with estimated $L_{\text{bol}} > 5 \times 10^{13} L_{\odot}$ in the optical, near-IR, and mid-IR to identify possible cases where the photometry used for the luminosity calculation was confused by nearby objects. Some sources

¹⁷ based on Figure 2, 3, and 4 of http://wise2.ipac.caltech.edu/docs/release/allsky/expsup/sec6_3a.html

Table 2
Photometry of *WISE* ELIRGs

Source	r' -band (μJy)	$3.6\mu\text{m}$ (μJy)	$4.5\mu\text{m}$ (μJy)	$12\mu\text{m}$ (mJy)	$22\mu\text{m}$ (mJy)	$70\mu\text{m}$ (mJy)	$160\mu\text{m}$ (mJy)	$250\mu\text{m}$ (mJy)	$350\mu\text{m}$ (mJy)	$500\mu\text{m}$ (mJy)
W0116–0505	10.2(0.5)	51(2)	89(1)	2.4(0.2)	12.1(1.1)	50(3)	93(6)	42(11)	<30	<42
W0126–0529	4.1(0.3)	33(2)	37(1)	1.0(0.2)	27.5(1.3)	29(2)	219(6)	213(10)	137(11)	71(14)
W0134–2922	...	38(8) ^b	99(11) ^b	5.0(0.2)	19.7(1.4)	36(3)	40(6)	46(12)	41(10)	50(11)
W0149+2350	<1.4	20(2)	35(1)	2.1(0.1)	9.8(0.8)	35(3)	91(4)	48(11)	89(16)	<57
W0220+0137	6.7(0.2) ^a	25(2)	38(1)	2.0(0.1)	12.4(1.0)	55(3)	120(6)	64(10)	56(11)	<42
W0255+3345	1.5(0.2) ^a	39(6) ^b	36(10) ^b	2.3(0.2)	16.5(1.2)	86(2)	73(7)	52(10)	42(10)	<42
W0410–0913	2.0(0.2) ^a	27(2)	46(1)	2.9(0.2)	13.4(1.2)	28(3)	110(6)	122(10)	117(11)	97(15)
W0533–3401	7.0(0.2) ^a	36(2)	73(1)	3.2(0.1)	12.0(1.0)	39(2)	98(10)	124(10)	85(10)	50(15)
W0615–5716	...	32(2)	49(1)	2.4(0.1)	15.0(0.8)	58(3)	110(6)	53(10)	37(11)	<42
W0831+0140	5.7(0.2) ^a	31(8) ^b	63(11) ^b	2.8(0.2)	10.3(1.1)	<35	<60	114(12)	93(10)	81(11)
W0858+4823	5.4(0.2) ^a	16(2)	45(1)	2.6(0.2)	12.2(1.3)	29(3)	63(10)	55(10)	57(11)	48(14)
W1248–2154	2.7(0.2) ^a	46(5) ^b	36(10) ^b	2.8(0.1)	13.1(0.9)	37(3)	67(2)	53(11)	36(10)	<42
W1322–0328	2.6(0.2) ^a	29(2)	60(1)	2.5(0.1)	11.5(1.1)	47(3)	64(7)	67(10)	47(11)	<39
W1838+3429	...	31(2)	35(1)	0.7(0.1)	8.4(0.9)	94(2)	38(7)	<27	<30	<42
W2042–3245	2.6(0.3) ^a	15(2)	19(1)	2.7(0.2)	16.4(1.3)	20(3)	30(5)	44(10)	<30	22(15)
W2201+0226	0.9(0.2) ^a	42(8) ^b	92(11) ^b	4.9(0.2)	18.1(1.4)	27(3)	141(7)	135(11)	138(12)	82(15)
W2210–3507	1.3(0.1) ^a	32(6) ^b	36(12) ^b	2.3(0.1)	16.5(1.0)	51(3)	140(6)	86(10)	95(11)	77(15)
W2246–0526	<3.9	28(2)	27(1)	2.5(0.2)	15.9(1.6)	37(3)	192(5)	89(9)	81(12)	44(15)
W2246–7143	...	22(4) ^b	17(6) ^b	1.4(0.1)	12.6(1.0)	29(3)	87(6)	71(9)	62(11)	31(15)
W2305–0039	0.6(0.2) ^a	58(6) ^b	67(11) ^b	3.4(0.2)	24.6(1.4)	83(10)	59(11)	44(15)

Note. — The numbers in parentheses are the $1-\sigma$ uncertainty in photometry. The upper limits are at $3-\sigma$.

^a Ground-based r' -band photometry from P. R. M. Eisenhardt et al. (in preparation).

^b Data from *WISE* $3.4\mu\text{m}$ or $4.6\mu\text{m}$ measurements.

from the low spectral resolution surveys (e.g. Iovino et al. 1996) showed *WISE* colors close to zero, much bluer than typical for quasars (Stern et al. 2012; Assef et al. 2013), and their SEDs resemble the thermal emission of stellar objects. Furthermore, the objects clustered at $z = 1.97 - 2.20$, triggering suspicions that their redshifts might be incorrect. Other quasars with unusual blue mid-IR colors such as J071046.20+473211.0 and J072810.14+393027.7 were removed due to known photometric contamination from nearby stars (Meisenheimer & Roeser 1983; Vigotti et al. 1997). Some of the sources have proper motions detected between the 2MASS and *WISE* observations, and their SEDs suggest they are likely late-type dwarf stars (e.g., J003332.60–392245.0, an M-type dwarf star; Plavchan et al. 2008) or known brown dwarfs (e.g., J144825.70+103158.0, an L3.5 brown dwarf; Wilson et al. 2003). After this culling from visual inspection, a total of 140 optically selected quasars reach the luminosity cut of $10^{14}L_{\odot}$, assuming their emission is isotropic.

To ensure that the intrinsic luminosities of the optically selected quasars are greater than the $10^{14}L_{\odot}$ threshold, we removed known gravitationally lensed systems and blazars. We invoked the catalog of strong gravitational lensing systems from “the Master Lens Database¹⁸” (L. A. Moustakas et al. in preparation), and the list of blazars from “the Roma-BZCAT Multi-frequency Catalogue of Blazars” (Massaro et al. 2009, version 4.1.1 – 2012 August). Of the 140 luminous quasars, 9 are in known strong gravitational lensing systems, and 15 are known blazars. This leaves a total of 116 hyperluminous quasars with $L_{\text{bol}} > 10^{14}L_{\odot}$, including 68 quasars from the SDSS DR7 quasar search (Schneider et al. 2010). These quasars are listed in Table 3.

To compare the far-IR SEDs of hyperluminous quasars

and Hot DOGs, we have gathered the available *Herschel* photometry for our quasar sample. *Herschel* SPIRE data are available for 15 quasars, and two of them also have PACS measurements. This photometry is listed in Table 4.

3. RESULTS AND ANALYSES

3.1. Color-Color Diagram

The *WISE* mid-IR color-color diagram at [3.4], [4.6], and [12] is shown in Figure 2. The *WISE*-selected ELIRG Hot DOGs occupy a wider range of [3.4]–[4.6] color than do the hyperluminous quasars, and the Hot DOGs are $\sim 2-3$ mag redder in [4.6]–[12] color. The Hot DOG redshifts span $2.8 < z < 4.6$, which is narrower than the quasar redshifts range of $0.9 < z < 4.9$. This is likely due, in part, to a selection effect which biases the Hot DOG selection to $z \gtrsim 1.5$ (Assef et al. 2015). The large gap between $4 < [4.6] - [12] < 5$ is a result of the *W1W2*-dropout selection criteria. Some hyperluminous objects have been discovered in this color region based on different mid-IR color selection criteria accompanied by criteria at other wavelengths (e.g., Bridge et al. 2013; Lonsdale et al. 2015; D. Stern et al. in preparation).

3.2. SEDs

The SEDs of the *WISE*-selected ELIRGs are shown in Figure 3, normalized by the integrated luminosity over the plotted SEDs. The SEDs of the $L_{\text{bol}} \geq 10^{14}L_{\odot}$ Hot DOGs are similar to those of their less luminous siblings, which are outlined by the shaded region. The steep rise from rest frame 1– $4\mu\text{m}$ reflects the selection criteria. These SEDs do not match empirical starburst or dusty AGN templates, although they are close to the torus model of Polletta et al. (2006). However, they are steeper than the torus model at $\lambda < 4\mu\text{m}$ and drop faster toward the far-IR at $\lambda > 60\mu\text{m}$. The rest-frame flux density peak is at shorter wavelengths than the peak of the

¹⁸ <http://www.masterlens.org/>

Table 3
Properties of Optically Selected Quasars with $L_{\text{bol}} > 10^{14} L_{\odot}$ (**Short Version**)

Source	WISE Coordinate		Redshift	$L_{\text{bol}}^{\text{a}}$ ($10^{14} L_{\odot}$)	Redshift Ref.
	R.A. (J2000)	Decl. (J2000)			
J000322.91–260316.8	00:03:22.91	–26:03:16.8	4.098	1.6	NED, V10
J001527.40+064012.0	00:15:27.40	+06:40:12.0	3.17	1.2	V10
J004131.50–493612.0	00:41:31.50	–49:36:12.0	3.24	1.8	V10
J010311.30+131618.0	01:03:11.30	+13:16:18.0	2.681	1.6	NED, V10
J012156.04+144823.9	01:21:56.03	+14:48:23.9	2.870	1.1	S10, V10
J012412.47–010049.8	01:24:12.47	–01:00:49.7	2.826	1.0	S10, P12, V10
J013301.90–400628.0	01:33:01.90	–40:06:28.0	3.023	1.0	V10
J015636.00+044528.0	01:56:36.00	+04:45:28.0	2.993	1.0	V10
J020727.20–374156.0	02:07:27.20	–37:41:56.0	2.404	1.2	V10
J020950.70–000506.0	02:09:50.71	–00:05:06.4	2.850	1.2	V10, S10, P12
J024008.10–230915.0	02:40:08.10	–23:09:15.0	2.225	1.4	V10
J024854.30+180250.0	02:48:54.30	+18:02:50.0	4.42	1.0	V10
J025240.10–553832.0	02:52:40.10	–55:38:32.0	2.35	1.2	V10
J030722.80–494548.0	03:07:22.80	–49:45:48.0	4.728	1.3	V10
J032108.45+413220.9	03:21:08.45	+41:32:20.8	2.467	1.1	S10

Note. — Redshifts from: V10 (Véron-Cetty & Véron 2010); C04 (Croom et al. 2004), C09 (Croom et al. 2009); S10 (Schneider et al. 2010); P12 (Paris et al. 2012), DR10 (Ahn et al. 2013), and NED (2013 April version of HyLIRG list from NASA/IPAC Extragalactic Database). Only the first 15 sources are listed here. The complete electronic table of 116 sources is available online at the journal website.

^a See Section 3.3 for definition.

Table 4
Photometry of Optically Selected Quasars with $L_{\text{bol}} > 10^{14} L_{\odot}$ (**Short Version**)

Source	R-band (mJy)	3.4 μm (mJy)	4.6 μm (mJy)	12 μm (mJy)	22 μm (mJy)	70 μm (mJy)	160 μm (mJy)	250 μm (mJy)	350 μm (mJy)	500 μm (mJy)
J000322.910–260316.80	0.40(0.11)	0.86(0.02)	0.69(0.02)	2.2(0.1)	8.5(0.9)
J001527.400+064012.00	0.43(0.12)	0.93(0.02)	1.09(0.03)	5.3(0.2)	10.9(1.1)
J004131.500–493612.00	0.79(0.22)	1.61(0.04)	1.62(0.04)	4.3(0.1)	9.1(0.8)
J010311.300+131618.00	1.09(0.30)	1.08(0.03)	1.51(0.04)	9.0(0.2)	19.4(1.0)
J012156.038+144823.94	0.31(0.09)	0.93(0.03)	1.16(0.03)	3.6(0.2)	9.2(1.0)
J012412.470–010049.76	0.45(0.12)	1.28(0.03)	1.40(0.03)	3.6(0.1)	6.7(1.0)
J013301.900–400628.00	0.49(0.13)	0.65(0.02)	0.89(0.03)	3.4(0.1)	9.4(0.9)
J015636.000+044528.00	0.43(0.12)	0.60(0.02)	0.67(0.02)	2.2(0.1)	3.1(0.8)
J020727.200–374156.00	0.85(0.23)	1.49(0.03)	1.71(0.04)	6.0(0.1)	12.3(0.8)
J020950.712–000506.49	0.63(0.17)	0.93(0.02)	1.36(0.03)	6.1(0.2)	15.0(0.8)	66(6)	48(6)	22(7)
J024008.100–230915.00	1.01(0.28)	1.92(0.04)	3.23(0.07)	11.1(0.2)	21.1(1.0)
J024854.300+180250.00	0.17(0.05)	0.62(0.02)	0.55(0.02)	1.6(0.1)	4.1(1.1)
J025240.100–553832.00	0.88(0.24)	1.73(0.04)	1.99(0.04)	8.2(0.2)	19.0(0.9)	46(2)	39(3)	14(3)
J030722.800–494548.00	0.06(0.02)	0.54(0.01)	0.51(0.02)	1.1(0.1)	4.0(0.7)
J032108.450+413220.87	0.56(0.15)	1.39(0.03)	1.94(0.05)	6.8(0.2)	12.7(1.1)

Note. — Only photometry of the first 15 sources are listed here. The complete electronic table with photometry of 116 sources is available online at the journal website. The numbers in parentheses are the $1-\sigma$ uncertainty in photometry.

dusty starburst system Arp 220, which is at about $60 \mu\text{m}$. This indicates emission from hotter dust in these *WISE*-selected hyperluminous galaxies. The emission excess around rest frame $6 \mu\text{m}$ can be explained by dust emission $T_d \sim 450$ K, as shown in the upper panel of Figure 3. This suggested temperature does not imply a single-temperature dust system, but is rather a characteristic temperature for the hot dust emission component. Further discussion of the SEDs and implied dust temperatures is included in Section 4.3.

3.3. Luminosity Estimates

The bolometric luminosity L_{bol} is calculated very conservatively by integrating over the photometric data, only considering $> 3\sigma$ detections, with a power law interpolated between observed flux density measurements, and extrapolated to 20% beyond the shortest and longest wavelength bands by assuming no luminosity beyond these wavelengths. We do not incorporate any extinc-

tion correction or SED model in our luminosity estimate. The resulting luminosity values from this approach can be considered as conservative lower limits. If the best-fit SED templates or spline-smoothed SEDs are considered, the luminosity values typically increase by a factor of 2.

The SEDs of the quasars do not extend to rest frame wavelengths $> 8 \mu\text{m}$ due to a lack of comprehensive far-IR data. The contribution to the bolometric luminosity at longer wavelengths is expected to be $< 35\%$ of the L_{bol} based on quasar SED templates (Polletta et al. 2006; Assef et al. 2010). Using available *Herschel* archival data, we estimate the contribution to L_{bol} by far-IR emission is $< 20\%$ for the optically selected quasars in this paper.

To estimate the luminosity contributed by different components to the SED, we separate the SED into three parts: rest-frame blue emission ($\sim 1000 \text{ \AA}$) to $1 \mu\text{m}$, emission from $1 \mu\text{m}$ to $20 \mu\text{m}$, and emission from $20 \mu\text{m}$ and beyond. The corresponding luminosities from these wavelength ranges are referred to as $L_{0.1-1 \mu\text{m}}$, $L_{1-20 \mu\text{m}}$,

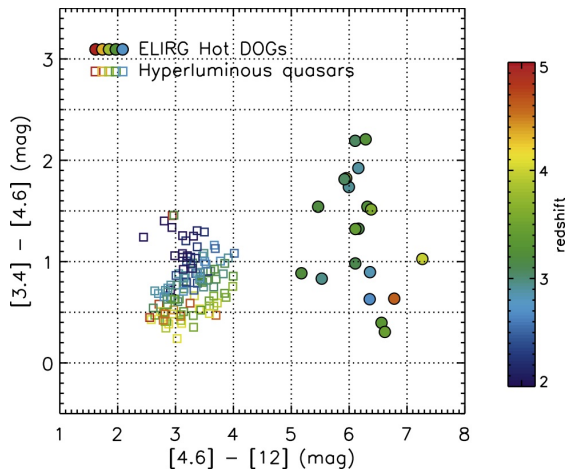


Figure 2. Mid-IR colors of the hyperluminous ($L_{\text{bol}} > 10^{14} L_{\odot}$) Hot DOGs and optically selected hyperluminous quasars. The open squares show the 116 selected quasars; the filled circles show the 20 *WISE*-selected Hot DOGs. For Hot DOGs not detected in *WISE* [3.4] and [4.6], their IRAC [3.6] measurements are plotted with the color correction from IRAC [3.6] to *WISE* [3.4] and IRAC [4.5] to *WISE* [4.6] applied.

and $L_{>20 \mu\text{m}}$, respectively. For simplicity, we refer to $L_{1-20 \mu\text{m}}$ as L_{MIR} hereafter. The $L_{>20 \mu\text{m}}$ should be distinguished from infrared luminosity, L_{IR} , which is defined as the accumulated luminosity between 8–1000 μm , and from the traditional far-infrared luminosity, L_{FIR} , which covers emission from 40 to 500 μm . The results are listed in Table 5.

4. DISCUSSION

The luminosity distributions of hyperluminous Hot DOGs and quasars are shown in Figure 4. The 20 luminous Hot DOGs have luminosities up to $10^{14.6} L_{\odot}$, reaching the same level as the non-lensed quasars, although the numbers are a factor of ~ 3 –5 lower without any consideration of selection effects. Assef et al. (2015) find that the space density of ELIRG Hot DOGs is comparable to the space density of extremely luminous unobscured quasars from SDSS-III BOSS (Ross et al. 2013) after correcting for the selection function used to identify Hot DOGs from *WISE* photometry and for spectroscopic incompleteness.

4.1. Possible Effects of Beaming?

The luminosities reported in this paper are calculated based on the assumption of isotropic emission in the observed wavebands. If the escaped energy is beamed, the intrinsic luminosity could be significantly overestimated. However, beaming, which is observed in blazars, is associated with variable light curves. In addition, Hot DOGs are only weakly detected or undetected in shallow (1 mJy), wide-area radio surveys (C.-W. Tsai et al. in preparation), unlike beamed objects which are typically radio bright (Urry & Padovani 1995).

Beaming implies small physical scales, hence the potential for rapid variability. We do not see significant variation in the *WISE* data. None of the Hot DOGs varies in *W3* and *W4* to a limit of 30% over 6 months, and none are flagged as significantly varying in the All-*WISE* catalog. Finally, many Hot DOGs have emission-line spectra (Wu et al. 2012; P. R. M. Eisenhardt et al. in

preparation), unlike the featureless spectral characteristic of BL Lac objects. These properties distinguish Hot DOGs from known beamed populations.

4.2. Possible Effects of Lensing?

Another possible explanation for the high luminosity of Hot DOGs is gravitational lensing by massive foreground systems. The most luminous known quasars, J0831+5245 and J1424+2256 with apparent $L_{\text{bol}} \gtrsim 10^{15} L_{\odot}$, are both gravitationally lensed (Lawrence et al. 1992; Patnaik et al. 1992; Irwin et al. 1998). For the *WISE* ELIRGs, while we cannot completely rule out the lensing hypothesis for these hyperluminous Hot DOGs, we consider the likelihood of strong lensing to be small based on the following arguments.

First, we consider what may be inferred from the *WISE* imaging data, estimating upper bounds on the possible magnification. Significant lensing requires the magnified source to be close to the effective Einstein radius (θ_{E}) of the lens. In general, θ_{E} is governed by the redshifts of background target and foreground lens, as well as the mass of the lens. In Case 1, θ_{E} is larger than the angular resolution of *W1* ($6''$). In Case 2, θ_{E} is smaller than $6''$ and the lensed images and foreground lens could be blended.

Case 1 is addressed by Figure 5, which shows the *W1* photometry vs. separation for objects in the 20 ELIRG fields. We use a SWIRE elliptical galaxy SED template and assume a total mass-to-light ratio of $M/L_B \sim 5$ in solar units (e.g. Faber & Gallagher 1979; Napolitano et al. 2005) to show the relationship between θ_{E} , *W1* photometry, and the mass of the lens. The maximum θ_{E} occurs near a lens redshift ~ 2.5 , for a source at $z = 3.2$ (the median ELIRG redshift), and the value of θ_{E} vs. *W1* for a lens at this redshift is shown by the solid blue line. Neighboring objects must be above this line to produce high magnification of the Hot DOG. No source falls above the line, and only one comes close. At the observed separations of *W1* objects in the ELIRG fields, such objects would need masses well above $10^{14} M_{\odot}$.

Galaxies with masses $> 10^{13} M_{\odot}$ exist, such as ESO 146-5 ($M \sim 10^{13} M_{\odot}$, Carrasco et al. 2010), which dominates the Abell 3827 cluster of galaxies, but massive galaxy clusters are not in evidence near the ELIRGs (Griffith et al. 2012; Assef et al. 2015). We conclude that the resolved individual *WISE* sources that we detect are not likely to be able to cause strong magnification of the ELIRGs.

There is the additional possibility that a much larger scale galaxy cluster potential could magnify ELIRGs near a correspondingly larger scale critical curve, which would not necessarily show extreme distortions or local multiple-images, particularly if the sources are quite compact intrinsically. However, the gravitational lensing magnification under this condition is usually small. Although the current optical and near-IR imaging data are not sufficient to fully explore that possibility, the *Spitzer* data do not show the aggregation of objects within $1'$ expected for a massive foreground lensing cluster of galaxies (Assef et al. 2015).

Case 2 is addressed by Figure 6, which shows the lens mass vs. redshift for a source at $z = 3.2$, the median redshift of the ELIRGs. In this case the lens would need to have $W1 > 16.8$ (or $< 58 \mu\text{Jy}$) to be consistent with

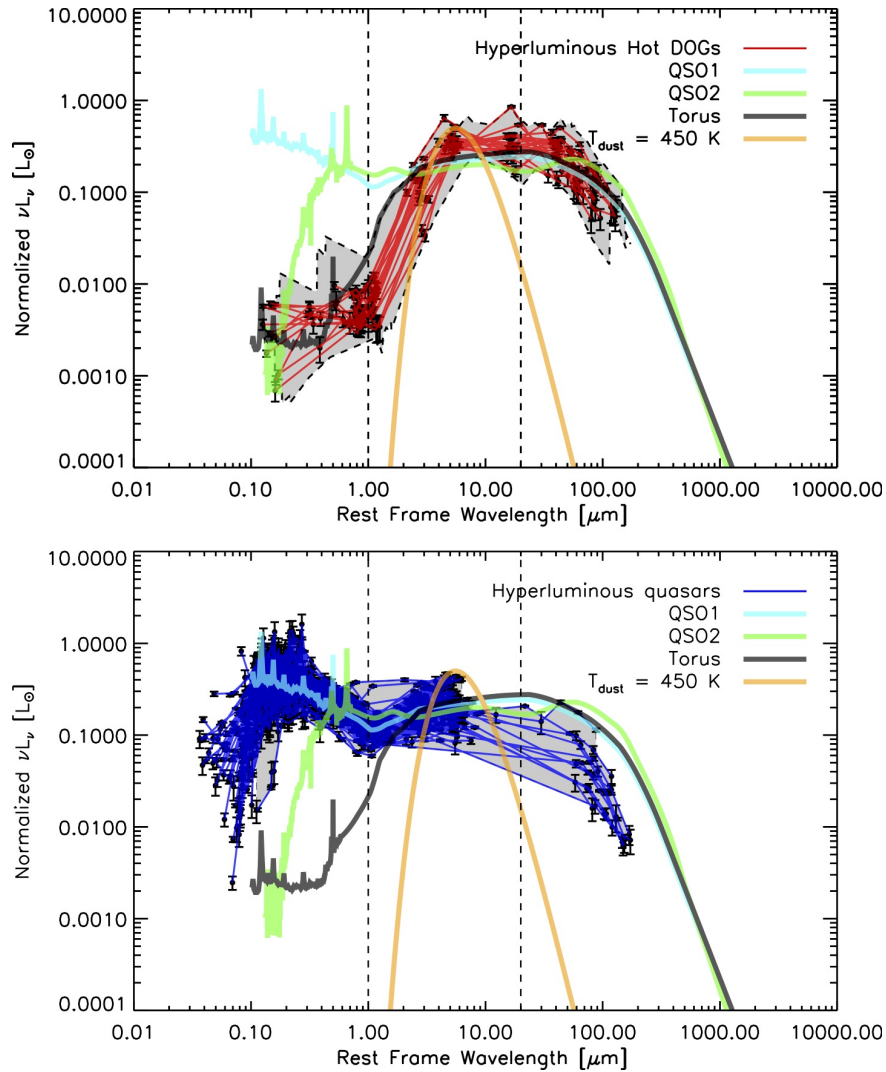


Figure 3. Normalized rest-frame SEDs of the hyperluminous ($L_{\text{bol}} > 10^{14} L_{\odot}$) ELIRG Hot DOGs and optically-selected hyperluminous quasars. The SEDs are normalized to the total bolometric luminosity L_{bol} . The shaded region in gray in the upper panel represents the scatter of SEDs for all Hot DOGs with $z > 1.6$ and $L_{\text{bol}} > 10^{13} L_{\odot}$, while the gray region in the lower panel covers the scatter of SEDs for the hyperluminous quasar sample. The plotted QSO and torus SED models are adopted from Polletta et al. (2006, 2007). The dust model line assumes a dust temperature $T_d = 450$ K with emissivity index $\beta = 2.0$. The vertical dashed lines indicate rest-frame wavelengths of 1 and $20 \mu\text{m}$.

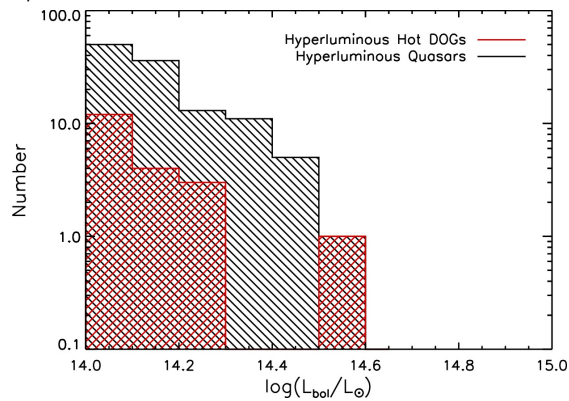


Figure 4. Luminosity histogram of $L_{\text{bol}} > 10^{14} L_{\odot}$ *WISE* Hot DOGs (in red) and optically selected quasars (in black). There are 20 Hot DOGs and 116 quasars in this plot.

the observed ELIRG data (see Table 2). As shown by the blue curve, this excludes $10^{12} M_{\odot}$ lenses up to $z = 1.5$, assuming $M/L_B \sim 5$. Lower mass lenses are possible, of course, but they must reach the critical mass surface density for gravitational lensing (see e.g. Subramanian & Cowling 1986). The remaining parameter space is highlighted as the gray shaded region in Figure 6. This parameter space can be investigated where we have high-resolution near-IR imaging.

We have obtained high angular resolution (PSF FWHM $\lesssim 0''.15$) near-IR imaging of over 30 Hot DOGs, including 6 ELIRGs reported in this paper, with the NIRC2 camera on Keck-II with adaptive optics, and with *HST*. These images do not show lensing features such as multiple images or arcs (Wu et al. 2014; S. M. Petty et al. in preparation; C. R. Bridge et al. in preparation). For the 5 ELIRGs in our sample with high-resolution near-IR imaging data, it is not uncommon to see other objects a few arcseconds from the ELIRGs in the images from

Table 5
Luminosities of *WISE* ELIRGs

Source	Redshift	L_{bol} ($10^{13}L_{\odot}$)	L_{IR} ($10^{13}L_{\odot}$)	$L_{0.1-1\mu\text{m}}$ ($10^{13}L_{\odot}$)	$L_{1-20\mu\text{m}}$ ($10^{13}L_{\odot}$)	$L_{>20\mu\text{m}}$ ($10^{13}L_{\odot}$)	$L_{5.8\mu\text{m}}$ ($10^{13}L_{\odot}$)	$L_{7.8\mu\text{m}}$ ($10^{13}L_{\odot}$)
W0116-0505	3.173	11.7	8.2	0.0	7.8	3.9	0.9	1.0
W0126-0529	2.937	14.7	10.7	0.1	7.0	7.6	1.8	1.3
W0134-2922	3.047	11.3	6.2	0.1	9.0	2.7	1.4	1.2
W0149+2350	3.228	10.4	7.4	0.0	6.2	4.1	0.8	0.8
W0220+0137	3.122	12.9	9.6	0.1	7.6	5.2	1.0	1.1
W0255+3345	2.668	10.4	7.9	0.0	6.8	3.6	0.9	1.1
W0410-0913	3.592	16.8	11.3	0.1	9.3	7.3	1.1	1.0
W0533-3401	2.904	10.4	7.5	0.1	5.7	4.6	0.8	0.8
W0615-5716	3.399	16.5	11.3	0.0	11.0	5.4	1.3	1.4
W0831+0140	3.888	18.0	12.0	0.2	11.0	7.1	1.1	1.1
W0859+4823	3.245	10.0	6.2	0.1	6.6	3.3	0.9	0.8
W1248-2154	3.318	11.8	7.4	0.1	8.0	3.6	1.0	1.0
W1322-0328	3.043	10.1	7.0	0.1	6.6	3.4	0.8	0.9
W1838+3429	3.205	11.1	8.9	0.1	8.6	2.5	0.9	1.4
W2042-3245	3.963	13.7	5.8	0.1	11.4	2.1	1.4	1.1
W2201+0226	2.877	11.9	8.0	0.0	6.6	5.5	1.2	0.9
W2210-3507	2.814	11.7	8.8	0.1	6.3	5.3	1.0	1.0
W2246-0526	4.593	34.9	22.1	0.1	22.2	12.6	1.9	1.8
W2246-7143	3.458	12.1	8.3	0.0	7.8	4.6	1.0	1.0
W2305-0039	3.106	13.9	8.3	0.0	10.1	3.8	1.7	1.4

Note. — The bolometric luminosity L_{bol} is conservatively estimated using power-laws to interpolate over photometry from r' -band to *Herschel* SPIRE [500] μm if applicable. See Section 3.3 for details. L_{IR} is the conventional infrared luminosity from rest-frame 8–1000 μm . $L_{0.1-1\mu\text{m}}$ is the luminosity from rest-frame 0.1–1 μm . $L_{1-20\mu\text{m}}$, which is also referred as L_{MIR} in this paper, covers 1–20 μm . $L_{>20\mu\text{m}}$ is the luminosity at wavelengths longer than 20 μm . $L_{5.8\mu\text{m}}$ and $L_{7.8\mu\text{m}}$ are the monochromatic luminosities at rest-frame 5.8 and 7.8 μm , respectively, estimated by interpolating the SEDs.

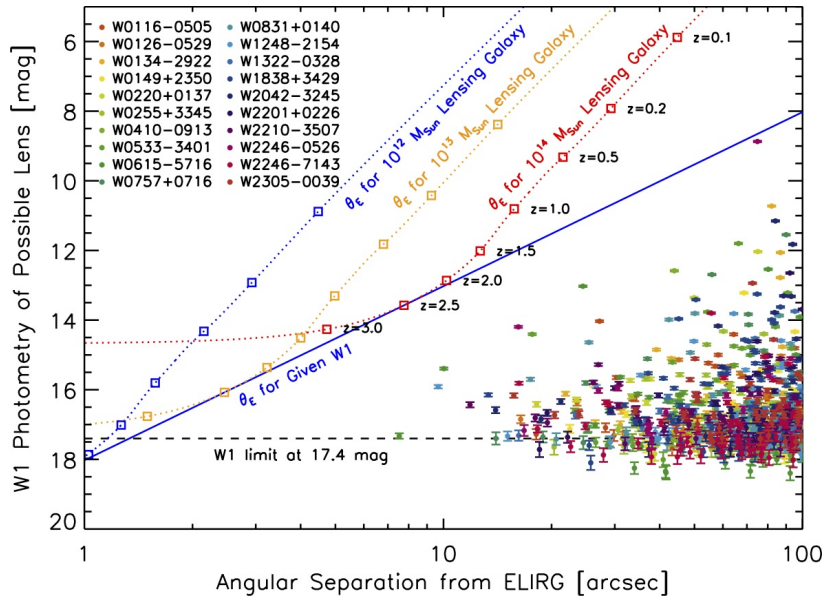


Figure 5. Photometry and angular separation of *WISE* W1 sources within $100''$ of the ELIRGs. Data points are color-coded by individual ELIRG as shown in the legend. The dashed black line at $W1 = 17.4$ mag shows the original selection limit for *WISE* Hot DOGs. The dotted lines show the Einstein radius (θ_E) and $W1$ magnitude (assuming $M/L_B \sim 5$ and using the elliptical galaxy SED template from Polletta et al. 2007) for lensing elliptical galaxies with different masses as labeled. Open squares along each dotted line mark representative lensing galaxy redshifts. The solid blue line represents the maximum θ_E vs. $W1$ for a source at $z = 3.2$, the median redshift of the 20 *WISE* ELIRGs, which occurs for a lens redshift of $z \sim 2.5$. *WISE* sources below the solid blue line are too faint and have too large an angular separation to be lenses.

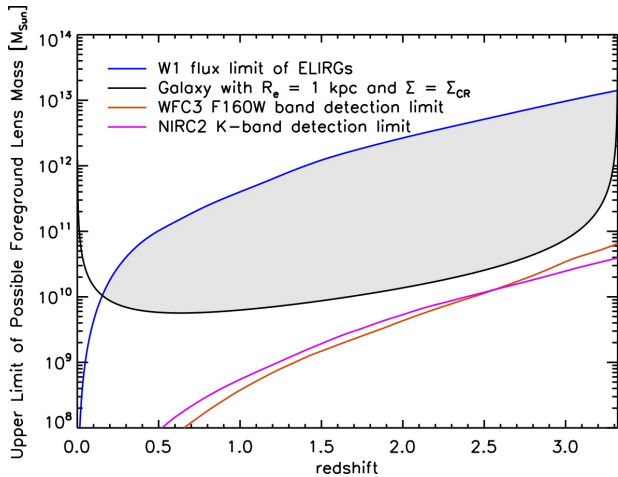


Figure 6. Mass limit of unresolved lenses vs. redshift, assuming a source at $z = 3.2$. The blue curve shows the upper limit due to the brightest $W1$ photometry ($W1 = 16.8$) observed for ELIRGs. The red-orange and magenta curves show the $3\text{-}\sigma$ detection limit of our high resolution imaging with *HST* WFC3 in F160W, and Keck NIRC2 with AO in the K -band. These curves are calculated using elliptical galaxy SED template from Polletta et al. (2007) with assumption of $M/L_B \sim 5$. The solid black line shows the mass of a lensing galaxy with size $R_e \sim 1$ kpc and surface mass density Σ equals to Σ_{CR} , the critical surface mass density necessary for gravitational lensing. The shaded region indicates the remaining lens galaxy mass parameter space.

HST or Keck with adaptive optics. However, these objects' morphologies are typical of recent or ongoing mergers, rather than characteristic lensing geometries, based on our experience with strong lensing work (Eisenhardt et al. 1996; Moustakas et al. 2007). There are sources which fall in the gray shaded area in Figure 6, but in no case is the θ_E corresponding to the inferred mass as large as their separation from the ELIRG. Thus, unless the lensing galaxies are anomalously faint or highly obscured, the high luminosity of Hot DOGs seems to be intrinsic rather than due to gravitational lensing.

We have also examined all of our 2D spectra. We have closely examined the 4 cases (W1248–2154, W2042–3245, W2246–0526, and W2246–7143) where nearby objects appear in the data (P. R. M. Eisenhardt et al. in preparation). Other than W1248–2154, discussed below, we have not identified any cases of two different redshifts superimposed that might be indicative of strong lensing (e.g. SLACS survey sample; Bolton et al. 2004, 2006). As discussed in detail below, we conclude that gravitational lensing is not causing the high luminosity of W1248–2154.

4.2.1. W1248–2154

Among the optical spectra of all 20 ELIRGs, only W1248–2154 suggests lensing. The spectrum of W1248–2154 shows two sources at $z = 0.339$ and $z = 3.326$ separated by $1''.3$ (P. R. M. Eisenhardt et al. in preparation). To explore the lensing hypothesis, we obtained K -band images of W1248–2154 using the NIRC2 camera with the Laser Guide Star Adaptive Optics (LGS-AO) system on the Keck II Telescope (van Dam et al. 2006; Wizinowich et al. 2006). WISE J1248–2154 was observed on the night of 2014 May 18 (UT) under good weather conditions. USNO-B star 0681-0325487 (Monet et al. 2003) with $R=16.9$ located $49''$ from the target was

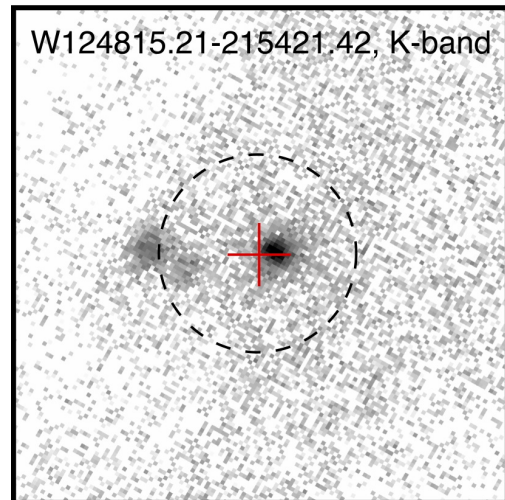


Figure 7. A $5'' \times 5''$ subsection of the Keck NIRC2 image of W1248–2154 in the K -band. The PSF FWHM is $\sim 0''.14$. The red cross shows the position of W1248–2154 from the AllWISE Catalog and the $0''.32$ uncertainty, which includes $0''.2$ registration uncertainty (1σ) of the K -band image and the $\sim 0''.25$ position uncertainty of W1248–2154 in AllWISE images. The black dashed circle indicates a $r = 1''$ region. The object on the right of the red cross is at $z = 3.326$, and the source on the left just outside the $r = 1''$ circle is at $z = 0.339$.

used for the tip-tilt reference. Images were obtained with the MKO K filter with field of view of $40'' \times 40''$ per frame and pixel scale of $0''.0397/\text{pixel}$. Thirty K -band images (120 sec per image) were obtained using a three-position dither pattern that avoided the noisy, lower-left quadrant. The total effective exposure time was 60 minutes.

The raw images were dark-subtracted and then sky-subtracted using a sky frame based on the median average of all frames, and a dome flat¹⁹ was used to correct for pixel-to-pixel sensitivity variations. The co-added image (Figure 7) is the median average of aligned single frame images based on the pixel location of a star in the field. The FWHM of point-like sources in the field is $\sim 0''.14$. The final NIRC2 image was registered to the seeing-limited J -band image from Assef et al. (2015), which has its WCS matched to the AllWISE WCS using $W1$ sources in the field of view.

The red cross in Figure 7 shows the AllWISE position of W1248–2154, which has an uncertainty of $0''.25$. The $0''.2$ extent of the cross indicates the astrometric uncertainty of the K -band image with respect to the AllWISE coordinate system. We do not find any significant gravitational lensing signatures in this image. We identify the brighter K -band source on the right of the cross as W1248–2154 at $z = 3.326$. The object to the left of the $r = 1''$ dashed circle is at $z = 0.339$. The source on the left just within the dashed circle is blended with the $z = 0.339$ object, and does not show noticeable spectroscopic features in our spectrum. The $z = 0.339$ object's K -band magnitude of ~ 22.4 mag corresponds to a lensing mass of $2 \times 10^9 M_\odot$, and an Einstein radius of $< 0''.12$, significantly smaller than the

¹⁹ Because of an issue with the lamp used to illuminate the spot for dome flats, we were unable to obtain K -band flats that night. Instead, we used the Keck Observatory Archive (<https://koa.ipac.caltech.edu>) to download K -band dome flats acquired on 2012 October 26 (PI: A. Cooray).

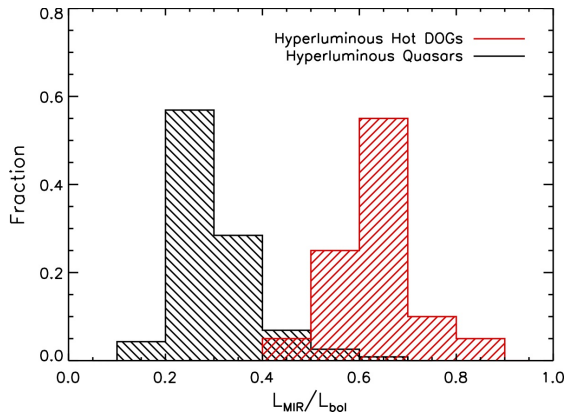


Figure 8. Normalized histogram of $L_{\text{MIR}}/L_{\text{bol}}$ for *WISE* Hot DOGs and optically selected quasars with $L_{\text{bol}} > 10^{14} L_{\odot}$, where L_{bol} is the total integrated luminosity calculated using power-law-connected SEDs and L_{MIR} is the integrated luminosity from 1 to $20 \mu\text{m}$.

separation between the companion and the ELIRG. So this foreground source is not producing strong lensing of the W1248–2154 Hot DOG. Thus we conclude that W1248–2154 is not a lensed system.

We also considered whether source confusion in the AllWISE mid-IR photometry might cause the luminosity for W1248–2154 to be overestimated. Like other Hot DOGs, the SED for W1248–2154 is dominated by the AllWISE photometry at 12 and $22 \mu\text{m}$. The $z = 0.34$ galaxy and $z = 3.3$ Hot DOG are blended in the AllWISE Atlas images. However, the separation is significantly larger than the $0''.25$ positional uncertainty of W1248–2154 in the AllWISE catalog. W1248–2154 does not have noticeable blending in the AllWISE catalog, suggesting that the foreground galaxy is not detected in the *W1* and *W2* bands. While we do not have 3 and $4 \mu\text{m}$ images with resolution better than the AllWISE *W1* images, the $z = 0.34$ source is significantly bluer than the $z = 3.3$ source between the *J*- and *K*-bands. Thus we believe that the foreground galaxy does not contribute significantly to the *W3* and *W4* photometry or the L_{bol} estimate for W1248–2154.

4.3. Dust Temperatures and SED Components

The Hot DOG SEDs generally peak between rest-frame 4 and $10 \mu\text{m}$ (see Figure 3), suggesting that the emitting dust can have temperatures up to $T_d \sim 450 \text{ K}$. The SED becomes Rayleigh-Jeans around $40\text{--}60 \mu\text{m}$, corresponding to $T_d \sim 60 \text{ K}$ (Wu et al. 2012; Bridge et al. 2013). Ground-based sub-millimeter follow-up observations of Hot DOGs indicate the rest-frame far-IR luminosity of Hot DOGs is about an order of magnitude lower than the rest-frame mid-IR luminosity (Wu et al. 2012; Jones et al. 2014). Considering the three SED components introduced in section 3.3, the blue component ($0.1\text{--}1 \mu\text{m}$) represents direct emission from the host galaxy, as well as direct or scattered emission from the AGN and its accretion disk; the mid-IR component ($1\text{--}20 \mu\text{m}$) represents emission from the AGN dust torus, or dust emission from the cocoon of highly obscured AGNs; and the $> 20 \mu\text{m}$ component represents far-IR emission from dust at the outskirts of the AGN, or starburst-powered dust emission from the host galaxy.

$L_{1\text{--}20 \mu\text{m}}$, or L_{MIR} as shown in Figure 8, is a better indicator of the hot dust-dominated luminosity of these hyperluminous systems, in contrast to the traditional infrared luminosity L_{IR} value which is more sensitive to diffuse dust emission powered by a starburst. As shown in Table 5, $L_{\text{MIR}} > L_{>20 \mu\text{m}}$ for every ELIRG. The bolometric contribution of emission blueward of $1 \mu\text{m}$ is negligible for the Hot DOGs and is likely redistributed by dust to rest-frame mid-IR wavelengths, resulting in the high $L_{\text{MIR}}/L_{\text{bol}} \sim 65\%$ (median value). In optically selected populations, especially the high luminosity quasars, L_{MIR} contributes only $\sim 30\%$ (median value) of L_{bol} .

Figure 9 shows νL_{ν} at $5.8 \mu\text{m}$ ($L_{5.8 \mu\text{m}}$) and $7.8 \mu\text{m}$ ($L_{7.8 \mu\text{m}}$), which have often been used to characterize AGN luminosities in the literature (e.g. Weedman et al. 2012). Common practice is to interpolate the SED to obtain these numbers, or to estimate them from an SED model. These numbers are convenient for statistical analyses such as deriving the quasar luminosity function. However, these monochromatic luminosities do not capture the variation in dust temperature distribution in different AGNs, which could be dramatic in obscured systems such as Hot DOGs. The ratios of $L_{5.8 \mu\text{m}}/L_{\text{bol}}$ and $L_{7.8 \mu\text{m}}/L_{\text{bol}}$ are substantially offset between ELIRG quasars and ELIRG Hot DOGs, and the scatter is large for both populations, particularly for quasars. The conversion from these monochromatic values to total L_{bol} can vary by a factor of ~ 3 (Figure 9). Hence we suggest that νL_{ν} at $5.8 \mu\text{m}$ or $7.8 \mu\text{m}$ as an estimate of total bolometric AGN luminosity should be used with caution.

4.4. Spatial Distribution of the Hot Dust

The extremely red SEDs of Hot DOGs suggests the extinction toward their central AGNs is very high, reaching $A_V \gtrsim 30 \text{ mag}$ (Eisenhardt et al. 2012; Stern et al. 2014; Assef et al. 2015). The absorbed energy is released at mid-IR wavelengths via thermal dust emission. As discussed in the previous two sections, the reprocessed energy (L_{MIR}) output in hyperluminous Hot DOGs dominates the total luminosity, and matches the luminosity emitted directly from the accretion disk ($L_{0.1\text{--}1 \mu\text{m}}$) in optically selected hyperluminous quasars. This enormous thermal dust luminosity suggests a dust covering fraction close to unity, rather than an edge-on dusty torus.

We estimate a dust sublimation radius (Barvainis 1987) of $\sim 8 \text{ pc}$ for the $\geq 10^{14} L_{\odot}$ Hot DOGs if they are heavily obscured by graphite-silicate mixed dust grains with a sublimation temperature of $\sim 1500 \text{ K}$. Here we assume that the bolometric luminosity is equal to the dust absorbed UV luminosity in these highly obscured systems. Unlike optically selected quasars, in which the variation timescale of optical emission is much shorter because the optical light comes directly from smaller physical scales (Schmidt 1963), the fluctuations of luminosity over time in Hot DOGs will be smoothed out by radiation reprocessing by the dust. The 16 pc diameter of the sublimation region sets the shortest variation timescale to be $\sim 50 \text{ yr}$ in the rest frame. However, the timescale for luminosity changes is more likely to be related to the scale of the dust that produces the peak emission in the SED. In Section 3.2, we show that the highest temperature dust and therefore smallest scale that contributes sub-

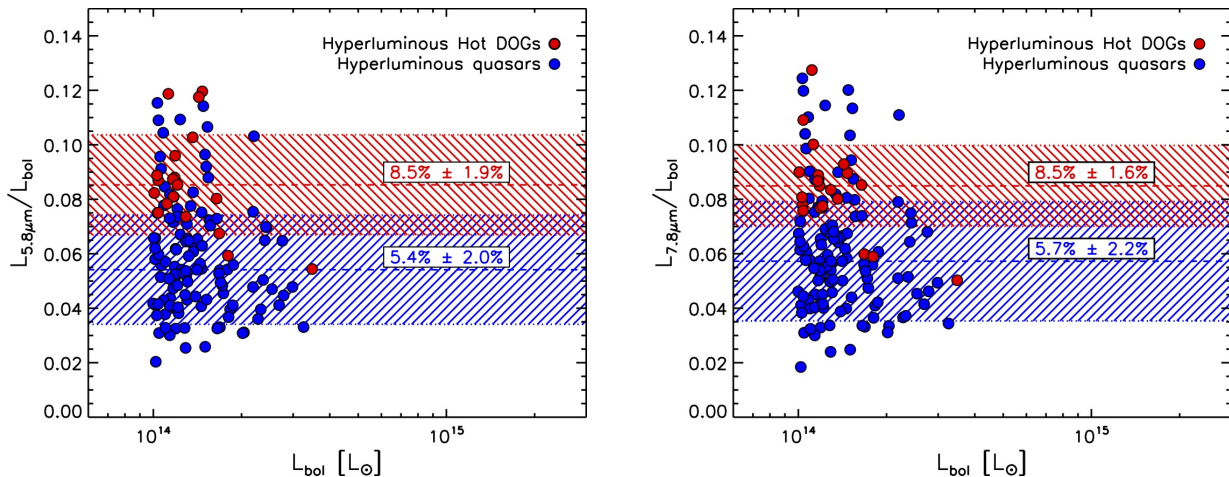


Figure 9. Ratio of $L_{5.8\mu\text{m}}$ to L_{bol} (*left*) and $L_{7.8\mu\text{m}}$ to L_{bol} (*right*) of hyperluminous Hot DOGs and quasars. The dashed lines represent the median values of luminosity ratios for Hot DOGs (red), and quasars (blue). The hatched regions show a 1σ range from the median value.

stantially to the SED is at a temperature of $T_d \sim 450$ K. If we assume the emitting dust is approximately in thermal equilibrium, the characteristic radius at that temperature is ~ 40 pc. Therefore we do not expect large luminosity variations over a rest-frame timescale less than ~ 200 yr, or many centuries in the observed frame. As noted in Section 4.1, the flux variation at 12 and $22\ \mu\text{m}$ is less than 30% over a 6-month period based on *WISE* observations.

4.5. Energy Source Other than AGNs?

In 200 years at $10^{14} L_{\odot}$, the total energy output is $\gtrsim 2.5 \times 10^{57}$ erg, or six orders of magnitude higher than the total energy output of a long gamma-ray burst (GRB, $E_{\text{total}} \sim 10^{51}$ erg). Rowan-Robinson (2000) argues that a starburst component is necessary for explaining the far-IR and submillimeter ($\lambda \geq 50\ \mu\text{m}$) SEDs of HyLIRGs. Could an extreme starburst provide this much energy for ELIRGs?

Without obvious starburst examples in the ELIRG luminosity range, we consider He 2-10, a local dwarf galaxy and a highly obscured starburst system, as an analogy to evaluate the possibility that the high luminosity is supported by star formation. In He 2-10, compact starburst regions are highly obscured and show mid-IR emission from hot dust (Beck et al. 2001). Beck et al. (2001) estimate an infrared luminosity $L_{\text{IR}} \sim 2 \times 10^5 L_{\odot}$ for the Lyman continuum photon rate $N_{\text{Lyc}} = 10^{49} \text{ s}^{-1}$ derived from radio measurements. If the obscured starburst case applies to the hyperluminous Hot DOGs, $10^{14} L_{\odot}$ would correspond to $N_{\text{Lyc}} \sim 5 \times 10^{57} \text{ s}^{-1}$.

We use the STARBURST99 simulation (Leitherer et al. 2010) with instantaneous starburst models to estimate the star formation needed to produce such a Lyman continuum photon rate. For a flat IMF (observed in compact starbursts in extreme environments such as young and massive clusters near the Galactic center – Figer et al. 1999, 2002), a total star formation of $\sim 2 \times 10^{10} M_{\odot}$ is needed, with higher masses for a Salpeter (1955) IMF. These must be formed within a few Myr – the lifetime of massive stars which produce most of the Lyman continuum photons. The implied star formation rate is $\text{SFR} > 5 \times 10^3 M_{\odot} \text{ yr}^{-1}$, at least an order of magnitude

higher than known extreme starburst systems such as sub-millimeter galaxies (Michalowski et al. 2010; Swinbank et al. 2014) or Lyman break galaxies (Shapley et al. 2005) at high redshift. Large masses of molecular gas and cold dust should accompany this level of star formation, but we observe neither substantial CO emission from these systems (A. Blain et al. in preparation) nor abundant cold dust (Wu et al. 2012; Jones et al. 2014). Thus we conclude, as did Eisenhardt et al. (2012), that a starburst is unlikely to be the dominant mechanism driving the high luminosity in Hot DOGs.

4.6. Black Hole Mass and Accretion History

Like quasars, Hot DOGs are likely powered by efficiently accreting SMBHs, albeit with extremely high obscurations. Here we consider the constraints on the mass and growth history of the SMBHs in the extremely luminous Hot DOGs and quasars based on their luminosities and redshifts. Below we show that the existence of ELIRGs at $z > 3$ implies SMBHs in ELIRGs have (1) a seed mass $\gg 10^3 M_{\odot}$; (2) a sustained super-Eddington accretion phase; or (3) a sustained radiation efficiency of $< 15\%$, producing less radiation feedback to limit accretion.

4.6.1. Current Eddington Ratio

The Eddington luminosity corresponds to the total emission from an isotropic accreting AGN when its radiation pressure is balanced by the gravitation of the SMBH. If we assume a hydrogen-dominated plasma, the SMBH mass at observed redshift z is thus

$$M_{\text{Eddington}} = M(z) \sim \frac{3 \times 10^9 M_{\odot}}{\epsilon(z)} \frac{L_{\text{bol}}}{10^{14} L_{\odot}}, \quad (1)$$

where $\epsilon(z)$ is the Eddington ratio.

If Hot DOGs are accreting below the Eddington limit the SMBH masses for ELIRGs are $> 3 \times 10^9 M_{\odot}$. This implies stellar masses $\sim 10^{12} M_{\odot}$ if the host galaxies follow the M - σ correlation, comparable to local giant elliptical galaxies in clusters. If $\epsilon(z) < 0.1$ for ELIRGs, the implied SMBH mass would be $M_{\text{BH}} \geq 3 \times 10^{10} M_{\odot}$, larger than the most massive SMBHs known in the local universe (McConnell et al. 2011). The lack of such

massive black holes at the present epoch is not easy to explain when the abundance of Hot DOGs matches that of powerful quasars (Assef et al. 2015), whose abundance is in turn consistent with the distribution of large elliptical galaxies today. Furthermore, if $M_{\text{BH}} > 10^{10} M_{\odot}$ for Hot DOGs, we would expect more massive host galaxies than observed unless Hot DOGs deviate substantially from the empirical $M - \sigma$ relation (Assef et al. 2015). While the extremely massive black holes and galaxy hosts expected for ELIRGs with low Eddington ratios are not found, there is some evidence that Hot DOGs are in rich environments. Follow-up observations using the SCUBA-II camera on JCMT show enhanced numbers of $850\mu\text{m}$ continuum sources within 1.5 of Hot DOGs (Jones et al. 2014), and *Spitzer* IRAC images also show enhanced densities of sources with red IRAC colors ($[3.6] - [4.5] > 0.37$), indicative of galaxies at $z \gtrsim 1$ (Assef et al. 2015).

Although super-Eddington accretion (i.e. $\epsilon(z) > 1$) is considered to be an unstable phase, it has been suggested to be common at $z > 1.7$ (Steinhardt & Elvis 2010). It is possible that Hot DOGs are in a transitional super-Eddington phase which produces their extraordinary luminosity. Indeed, super-Eddington accretion is commonly invoked to explain the non-nuclear ‘‘ultraluminous X-ray’’ (ULX) source populations seen in local galaxies (e.g., Bachetti et al. 2014). However, super-Eddington accretion requires a special configuration for the accretion disk, and the timescales for super Eddington accretion in AGN are not thoroughly investigated and understood. Begelman (2002) suggests that the Eddington limit can be exceeded by 10–100 times via small scale inhomogeneities in the thin disk accretion. Ohsuga & Mineshige (2007) suggest accreting material through the photon trapping regions around the accreting black hole can help the system stably bypass the radiation feedback. Statistical study of SDSS quasars suggests the maximum Eddington ratio for Type 1 quasars is $\epsilon \sim 3$ (Kelly & Shen 2013), though Hot DOGs could be in a different accretion phase from Type 1 quasars.

At high Eddington rates, the black hole mass in ELIRGs can grow by an order of magnitude over 10^7 yr, much faster than the growth of stellar bulges. The relatively tight $M - \sigma$ relation seen in the local universe suggests that high Eddington rate phases do not account for a significant fraction of cosmic SMBH mass growth.

4.6.2. Time-averaged Eddington Ratios and Radiation Efficiency

The ELIRG Hot DOG systems are at $z > 2.5$, leaving the SMBHs in them < 3 Gyr to grow to the mass at which we observe them. Based on the arguments of Shapiro (2005), we can estimate the time-averaged Eddington ratio in these systems. In the following discussion, we do not consider BH mass growth via BH mergers, although these may play a role at high redshift when the BH density is relatively high. However, the merging timescale, driven by the coalescence timescale of stellar relaxation of host galaxies, is much longer than the Salpeter timescale for BH mass growth by accretion. Thus, compared to mass accretion, mass increase by mergers plays a relatively minor role in BH mass growth history.

For a black hole with mass $M_{\text{BH}}(z)$ at redshift z , accretion rate \dot{M}_{acc} , black hole mass growth rate \dot{M}_{BH} , and

radiative efficiency $\eta(z)$, the observed luminosity at redshift z is

$$L(z) = \eta \dot{M}_{\text{acc}} c^2 = \frac{\eta \dot{M}_{\text{BH}}}{(1 - \eta)} c^2. \quad (2)$$

We can also relate the observed luminosity to the Eddington luminosity,

$$L(z) = \epsilon(z) L_{\text{Edd}} = \epsilon(z) a M_{\text{BH}}(z) \quad (3)$$

where ϵ_z is the Eddington ratio, and a is a constant associated with the opacity of accreting materials. By combining Eq. 2 and Eq. 3 with cosmic time $t(z)$, one can derive

$$\frac{dM_{\text{BH}}}{dt} = \epsilon(t)(1 - \eta) \frac{a}{\eta c^2} M_{\text{BH}} = \frac{\epsilon(t) M_{\text{BH}}}{\tau_{\text{Salpeter}}}. \quad (4)$$

The factor $\tau_{\text{Salpeter}} \equiv \frac{\eta c^2}{(1 - \eta)a}$ is the Salpeter (1964) timescale, which describes the time span for an e-fold mass increase of a black hole accreting at its Eddington limit. For a hydrogen-dominated plasma, $a \simeq 3.3 \times 10^4 L_{\odot}/M_{\odot}$, and with $\eta = 0.057$ for a Schwarzschild black hole (Bardeen et al. 1973) rather than the more commonly adopted empirical value of 0.1 (Yu & Tremaine 2002), τ_{Salpeter} is ~ 50 Myr. For a Kerr black hole where $\eta = 0.3$ (Thorne 1974), $\tau_{\text{Salpeter}} \sim 192$ Myr. In other words, a non-spinning black hole experiences less radiation feedback to accreting material due to its lower radiation efficiency, thus its mass doubling time could be $\gtrsim 3$ times shorter than a fast spinning black hole.

Assuming black holes of seed mass M_{seed} appear at $z \sim 20$ (Couchman & Rees 1986; Bromm et al. 2009), the age of the black holes since their appearance is $T_{\text{age}}(z) \equiv \int_z^{z \sim 20} dt$, and the time-averaged Eddington ratio $\bar{\epsilon}(z)$ is

$$\bar{\epsilon}(z) \equiv \frac{\int_z^{z \sim 20} \epsilon(t) dt}{\int_z^{z \sim 20} dt} = \frac{\int_z^{z \sim 20} \epsilon(t) dt}{T_{\text{age}}} \quad (5)$$

between $z \sim 20$ and redshift z . Thus, from Eq. 4, we derive that the evolution of black hole mass M_{BH} can be written as

$$\begin{aligned} \ln \left(\frac{M_{\text{BH}}(z)}{M_{\text{seed}}} \right) &= (1 - \eta) \frac{a}{\eta c^2} \int_z^{z \sim 20} \epsilon(t) dt \\ &= \bar{\epsilon}(z) \frac{T_{\text{age}}(z)}{\tau_{\text{Salpeter}}}, \end{aligned} \quad (6)$$

and

$$\bar{\epsilon}(z) = \ln \left(\frac{L(z)}{\epsilon(z) L_{\text{Edd}}(M_{\text{seed}})} \right) \left(\frac{T_{\text{age}}(z)}{\tau_{\text{Salpeter}}} \right)^{-1}. \quad (7)$$

For the ELIRG Hot DOGs at $2.8 \lesssim z \lesssim 4.6$, we assume the current value $\epsilon(z) \sim 1$ (see discussion of Section 4.6.1). The age of the Universe at that redshift is ~ 1.4 – 2.4 Gyr. If M_{seed} of the SMBHs in these systems is of order 10 – $100 M_{\odot}$ as suggested by simulations of SMBH seeds from population III stars (Zhang et al. 2008; also see review by Volonteri 2010), the derived time-averaged Eddington ratios of our systems are $\bar{\epsilon} \sim 0.71$ ($z = 4.6$) or ~ 0.46 ($z = 2.8$). We note that the uncertainties in assumptions on $\epsilon(z)$, M_{seed} , and $L(z)$ do not affect

the $\bar{\epsilon}$ estimate significantly due to the logarithmic scaling (Equation 7). An order of magnitude uncertainty in these parameters will change the estimate of $\bar{\epsilon}$ by 0.1 at the most. T_{age} depends on when SMBH seeds appear ($z \sim 20$), so the maximum possible T_{age} would decrease $\bar{\epsilon}$ by less than 0.15. Differences in τ_{Salpeter} will affect $\bar{\epsilon}$. The higher η of rapidly spinning black hole results in even higher value of $\bar{\epsilon}$. The same arguments apply to the ELIRG quasars in the same redshift range. Thus, the time-averaged Eddington ratios $\bar{\epsilon}$ of the ELIRG systems we discuss here are securely larger than 25%. In comparison, the most massive black hole known so far with $\sim 2 \times 10^{10} M_{\odot}$ (McConnell et al. 2011) would have $\bar{\epsilon} \sim 0.07$ over the Hubble time.

4.6.3. Seed Black Hole Mass and Black Hole Spin

The previous section discusses a simple model of M_{BH} growth history (Equation 6) in which the variables are the seed black hole mass M_{seed} , the radiative efficiency η , and the Eddington ratio $\epsilon(z)$. Current models suggest seed black hole masses ranging from $\sim 10M_{\odot}$ from simulations of the end products of population III stars (e.g., Zhang et al. 2008) to $\sim 100M_{\odot}$ from run away collisions between stars in dense clusters (e.g., Begelman & Rees 1978) to as much as $10^6 M_{\odot}$ for supermassive stars that quickly accumulate ambient material and collapse into black holes (Wise et al. 2008; Regan & Haehnelt 2009).

Figure 10 shows L_{bol} vs. z for hyperluminous Hot DOGs and quasars, and for quasars at $z > 6$. The curves in the figure show the luminosity vs. redshift tracks followed by black holes as they grow for various choices of M_{seed} and η . Although in reality the Eddington ratio ϵ is likely to vary, the overall averaged Eddington ratio $\bar{\epsilon}$ should be lower than unity. With the assumption of $\epsilon \sim 1$ constantly, we consider cases with $\eta \sim 0.1$, a commonly adopted value for a slowly spinning or non-spinning black hole, $\eta \sim 0.2$ for an intermediate spinning black hole, and $\eta \sim 0.3$ for a rapidly spinning black hole. The radiative efficiency is a factor of 3 higher for a Kerr black hole because the material can still radiate gravitational energy to the last stable circular orbit, which is 3 times smaller compared to a non-spinning Schwarzschild black hole or a slowly spinning black hole (Thorne 1974). The curves on Figure 10 represent the theoretical limits of black hole mass growth, and the objects toward the upper right of the curves can not be produced with the given initial seed mass and radiative efficiency unless the SMBH is in a super-Eddington state for a significant period of its history.

If $\eta \sim 0.2$ – 0.3 is adopted, the higher radiative efficiency means that the SMBH accumulates less mass to produce the same luminosity. Assuming black hole merging is not important, black holes with $\eta = 0.3$ can not produce the observed ELIRGs and $z > 6$ quasars unless their seed mass $M_{\text{seed}} \gg 10^4 M_{\odot}$ or/and they have been accreting at super-Eddington rates since their formation in the early Universe. For the most luminous Hot DOGs and quasars, the required seed mass is $M_{\text{seed}} > 10^7 M_{\odot}$, higher than the most massive seed masses predicted by current models (Begelman et al. 2008; Agarwal et al. 2012; Hosokawa et al. 2013). On the other hand, for $\eta = 0.1$ (dotted lines in Figure 10), relatively modest seed black holes can grow to Hot DOGs if they are accreting at $\epsilon(z) > 0.4$. If the seed mass exceeds $10^4 M_{\odot}$,

even accretion rates $\epsilon < 0.1$ can appropriately create hyperluminous quasars at $z > 6$, and ELIRGs at $z < 5$.

Under the conservative assumption of constant accretion at the Eddington limit since $z = 20$, the existence of hyperluminous Hot DOGs and quasars at $z > 3.5$ implies a constraint on the upper limit to the radiative efficiency for given seed black hole mass values. In Figure 11, we show the upper limits of radiative efficiency in the cases of $M_{\text{seed}} = 10^3 M_{\odot}$ and $M_{\text{seed}} = 10^6 M_{\odot}$. The first case represents the upper bound on the predicted black hole seed mass from the first stars (Hirano et al. 2014, and references therein). The $10^6 M_{\odot}$ case is upper bound of the seed mass from direct collapse of pristine gas clouds (Agarwal et al. 2012), or from rapid mass accretion onto primordial massive stars (Hosokawa et al. 2013). The hyperluminous Hot DOGs and quasars at $z > 3.5$ place similar constraints on black hole radiative efficiency η as $z > 6$ quasars. If the black hole seeds have masses of $\sim 10^3 M_{\odot}$, we expect that SMBHs have radiative efficiency on average lower than 15% to form the ELIRGs and hyperluminous quasars at $z > 4$. If a higher seed mass is adopted, the upper limits of η are still $< 25\%$, which corresponds to the radiative efficiency of a mildly rotating black hole. This suggests that the SMBHs in these most luminous systems are either (1) born with high mass (as discussed by Johnson et al. 2013, for quasars at $z > 7$), (2) experience substantial super-Eddington accretion episodes in their growth history (Kelly & Shen 2013), or (3) have sustained lower radiation feedback to accretion due to lower radiation efficiency for slowly spinning black holes. In the latter case, some mechanism, such as accretion with randomized directions (King & Pringle 2006; King et al. 2008; Fanidakis et al. 2012), has to interrupt the increase of black hole spin by angular momentum transported from a regulated accretion disk, otherwise a black hole can be spun up close to the theoretical limit over a few Salpeter timescales.

4.7. High Luminosity State Time Scale

Analysis of the black hole mass function at $z = 0$ suggests that SMBHs spend $\sim 1\%$ of their lifetime in a luminous, high accretion rate mode, and 99% in a dim, low accretion phase (Hopkins et al. 2006b). The high accretion phase dominates the BH mass growth. For ELIRGs, the accretion rate \dot{M} required to radiate at the ELIRG luminosity level is $\dot{M} = L/(\eta c^2) \sim (7/\eta) M_{\odot} \text{yr}^{-1}$. For the typical $\eta = 0.1$ radiative efficiency of a slow-spinning black hole, $\dot{M} \sim 70 M_{\odot} \text{yr}^{-1}$.

The minimum lifetime of the high luminosity phase in hyperluminous Hot DOGs can be estimated by considering the depletion time of the observed dusty material. The peak of the ELIRG SEDs suggests that the luminosity is dominated by radiation from hot dust at $T_d \sim 450$ K. At that temperature, the required dust mass to produce the observed $L_{\text{MIR}} \sim 8 \times 10^{13} L_{\odot}$ is on the order of $2700 M_{\odot}$. This dust mass is just ~ 40 times the mass annually accreted by the SMBH in Hot DOGs. This timescale is shorter than the light-crossing time scale of 200 yr discussed in Section 4.4.

On the other hand, Assef et al. (2015) have studied the luminosity functions of Hot DOGs and luminous quasars, finding they have comparable number density. This sug-

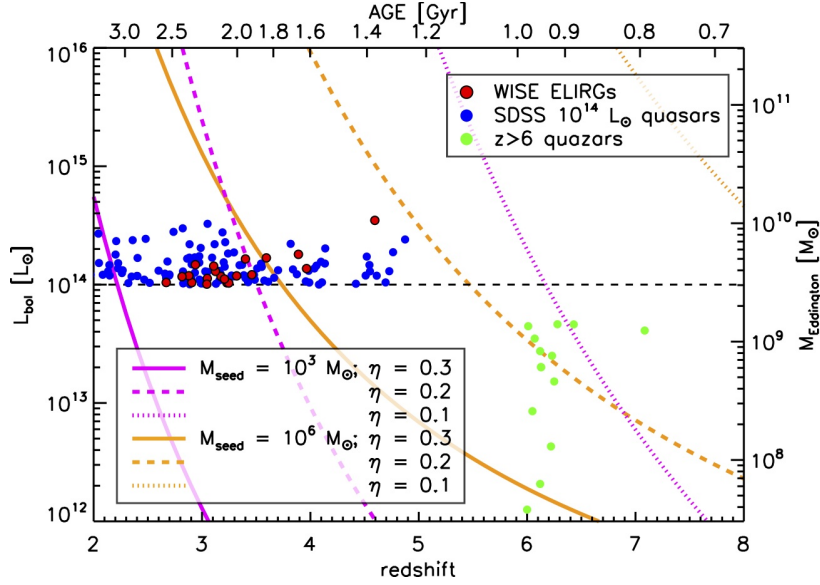


Figure 10. Bolometric luminosity L_{bol} vs. redshift. The age of the SMBH since formation at $z \sim 20$ is plotted on the top. The black hole mass for an Eddington ratio of one ($\bar{\epsilon} = 1$) is plotted on the right. The dotted, dashed, and solid curves are the black hole accretion history between $z = 8$ and $z = 2$ for $\bar{\epsilon} = 1$ and radiative efficiency $\eta = 0.1, 0.2,$ and 0.3 , respectively. The magenta lines show predictions with initial black hole mass $M_{\text{seed}} = 10^3 M_{\odot}$, while yellow lines show the case of $M_{\text{seed}} = 10^6 M_{\odot}$. The regions to the top and right of each curve require significant periods of super-Eddington accretion for the curve’s seed mass and radiative efficiency. The red dots show ELIRG Hot DOGs, the blue dots show ELIRG quasars, and the green dots show resulting quasars at $z > 6$ based on Blain et al. (2013, and references therein).

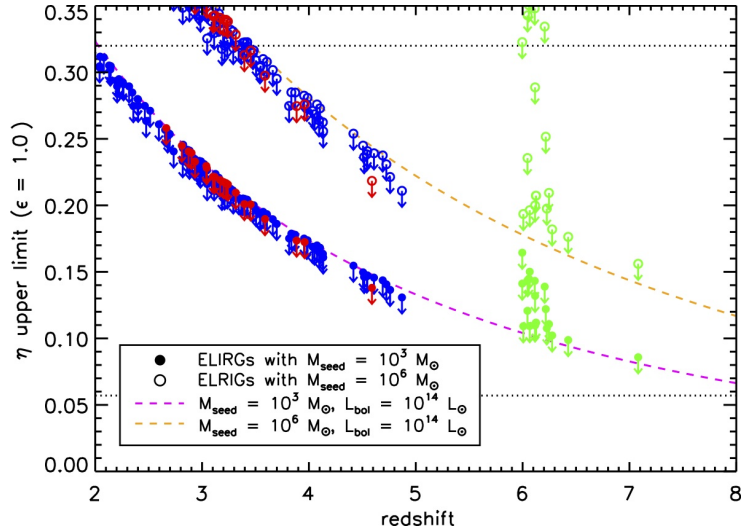


Figure 11. Upper limits on radiative efficiency implied by hyperluminous Hot DOGs, quasars, and high redshift ($z > 6$) quasars (color coded as in Figure 10). Black holes radiating too high a fraction of their accreted mass cannot grow large enough to produce the observed luminosities at the Eddington limit. The filled circles and magenta lines show cases with initial black hole seed mass $M_{\text{seed}} = 10^3 M_{\odot}$, and open circles and yellow lines show $M_{\text{seed}} = 10^6 M_{\odot}$. The dashed lines outline the luminosity threshold of $L_{\text{bol}} > 10^{14} L_{\odot}$ used in this paper. The horizontal dotted lines are the theoretically predicted radiative efficiency of a non-spinning black hole ($\eta = 0.057$) and a highly spinning black hole ($\eta = 0.32$). All the lines and dots are plotted assuming a constant Eddington ratio $\epsilon = 1$.

gests similar lifetimes for both the obscured and the unobscured phases of hyperluminous black hole accretion. Using the life cycle of broad line quasars at $z = 1$ (Kelly et al. 2010) as an analog, this time scale is ~ 100 Myr, likely to be the upper bound for Hot DOG phase. This timescale is a few times the Salpeter timescale. The accreted mass onto the SMBH exceeds $7 \times 10^9 M_{\odot}$.

4.8. A Luminosity Limit at $L_{\text{bol}} \sim 10^{14.5} L_{\odot}$?

Our systematic search for ELIRGs using the “W1W2-dropout” selection criteria has identified about 1000 candidates in the *WISE* database (Eisenhardt et al. 2012). Among the 150 of these candidates from which we have redshift information, a total of 20 ELIRGs at $z > 2.5$ have been discovered as reported in this paper, including the most luminous system, W2246–0526 at $z = 4.593$ with $L_{\text{bol}} \sim 3.5 \times 10^{14} L_{\odot}$.

Are there other infrared objects, either starbursts or obscured AGNs, with similarly high luminosities? Re-

cently, 1HERMES X24 J161506.65+543846.9 at $z = 4.952$ was discovered by *Herschel* HerMES survey (Casey et al. 2012a). Its L_{IR} is reported to be $\sim 1.2 \times 10^{14} L_{\odot}$ based on an SED model with $T_{\text{dust}} = 98 \text{ K}$. It is the brightest object in their sample, and tentatively classified as a starburst system based on its optical spectrum (Casey et al. 2012a). Our conservative estimate using *WISE* and *Herschel* photometry would imply its L_{bol} is $\sim 8 \times 10^{13} L_{\odot}$, slightly shy of our L_{bol} threshold, but likely making it one of the most powerful starburst systems known. In addition to *Herschel* studies, a few systems discovered by *WISE* using different selection criteria have L_{bol} at the $\sim 10^{14} L_{\odot}$ level (Lonsdale et al. 2015; D. Stern et al. in preparation), but they all show obvious AGN features in their spectra or have radio emission.

The $L_{\text{bol}} \sim 10^{14.5} L_{\odot}$ of W2246–0526 exceeds the most luminous quasars listed in Table 3 (see Figure 4). Could there be even more luminous Hot DOGs?

In Figure 10, a few quasars at $z > 6$ have implied black hole mass $\gtrsim 10^9 M_{\odot}$ at an age of $< 1.0 \text{ Gyr}$. If they accrete at the Eddington limit, they could potentially reach $> 10^{15} L_{\odot}$ by $z \sim 5$. Thus far, we have not observed any system at that L_{bol} level. Such systems are expected to be rare: no more than a few over the whole sky based on the luminosity function of Hot DOGs and optical quasars. At $z > 5$, the hot dust emission peak at $6 \mu\text{m}$ will shift to $\sim 40 \mu\text{m}$, well beyond the *WISE* $22 \mu\text{m}$ (*W4*) filter. To identify such sources would require deeper imaging at $30\text{--}70 \mu\text{m}$ from future missions such as *SPICA*, or submillimeter photometry at $200 \mu\text{m}$ – 1 mm with ALMA or CCAT. As noted by Assef et al. (2015), such objects may also have been detected by *WISE* but failed to meet the *W1W2*-dropout selection, because they will be detectable by *WISE* at 3.4 and $4.6 \mu\text{m}$. If we relax the *W1* and *W2* flux limits for Hot DOGs, many contaminants fall into the selection criteria, making it much more difficult to identify the ELIRG systems. It is also possible that AGN at $\sim 10^{14.5} L_{\odot}$ have reached a physical limit for BH accretion, or that the accreting material is depleted after $z \sim 5$. If so, this might explain the upper luminosity bound at $10^{14.5} L_{\odot}$ for hyperluminous Hot DOGs and quasars in Figure 10.

5. SUMMARY

We report 20 highly obscured, ELIRG AGNs discovered by *WISE*. These sources, because of their similarity to DOGs with steeply rising SEDs towards the mid-IR albeit with hotter dust components, have been dubbed Hot DOGs by Wu et al. (2012). The luminosities of these objects exceed $10^{14} L_{\odot}$, making them among the most luminous (non-transient) systems in the universe. They are not likely to be powered by starbursts, but rather by highly obscured and actively accreting AGNs. Based on their lack of variability and the absence of evidence for foreground lensing systems in their spectra and images, we conclude that the high luminosity is generally not a result of relativistic beaming or gravitational lensing.

We present the full SED of these objects from observed optical to far-IR wavelengths. For both hyperluminous Hot DOGs and unobscured quasars of similarly high luminosity, we show that the conversion from monochromatic mid-IR luminosity to total L_{bol} can vary by a factor of ~ 3 . Thus, the use of single-wavelength νL_{ν} values such as $L_{5.8 \mu\text{m}}$ and $L_{7.8 \mu\text{m}}$ to represent L_{bol} needs to

be reevaluated considering dust obscuration and thermal dust emission.

Based on the Hot DOG SEDs, we suggest that emission from a dust component at $T_d \sim 450 \text{ K}$ contributes the majority of the luminosity. This dust component, with a characteristic radius of $\sim 40 \text{ pc}$, contains $2700 M_{\odot}$. Because of its physical size, we expect that large flux variations in these Hot DOGs should not occur on timescales $\lesssim 200 \text{ yr}$.

The high luminosities in the ELIRG Hot DOGs are likely maintained by $M_{\text{BH}} \sim 3 \times 10^9 M_{\odot}$ SMBHs accreting near the Eddington limit. Their existence at redshift $2.8 < z < 4.6$ implies a time-averaged Eddington ratio of $> 25\%$ up to their observed epochs. It would be difficult for these SMBHs to grow to $10^9 M_{\odot}$ with the relatively high radiative efficiency $\epsilon \sim 0.3$ expected from a Kerr black hole. This suggests that the spin of SMBHs in Hot DOGs may be low, perhaps as a result of chaotic accretion due to galaxy merger events.

Note added in proof. – After this paper was submitted, we were alerted to the discovery of SDSS J0010+2802 at $z = 6.3$ with $M_{\text{BH}} \sim 1.2 \times 10^{10} M_{\odot}$ (Wu et al. 2015). Using our methodology, the luminosity of this source is $1.6 \times 10^{14} L_{\odot}$.

The authors thank the anonymous referee for the constructive comments and for encouraging a more thorough discussion of gravitational lensing in this paper. This publication makes use of data products from the *Wide-field Infrared Survey Explorer*, which is a joint project of the University of California, Los Angeles, and the Jet Propulsion Laboratory/California Institute of Technology, and *NEOWISE*, which is a project of the Jet Propulsion Laboratory/California Institute of Technology. *WISE* and *NEOWISE* are funded by the National Aeronautics and Space Administration. This work is also based in part on observations made with the *Spitzer Space Telescope*, which is operated by the Jet Propulsion Laboratory, California Institute of Technology under a contract with NASA. Some of the data presented herein were obtained at the W.M. Keck Observatory, which is operated as a scientific partnership among the California Institute of Technology, the University of California and the National Aeronautics and Space Administration. The Observatory was made possible by the generous financial support of the W.M. Keck Foundation. Part of this research has made use of the Keck Observatory Archive (KOA), which is operated by the W. M. Keck Observatory and the NASA Exoplanet Science Institute (NExScI), under contract with the National Aeronautics and Space Administration. This research has made use of the NASA/IPAC Infrared Science Archive and the NASA/IPAC Extragalactic Database (NED), which are operated by the Jet Propulsion Laboratory, California Institute of Technology, under contracts with the National Aeronautics and Space Administration. This material is based upon work supported by the National Aeronautics and Space Administration under Proposal No. 13-ADAP13-0092 issued through the Astrophysics Data Analysis Program. C.-W. T. was supported by an appointment to the NASA Postdoctoral Program at the Jet Propulsion Laboratory, administered by Oak Ridge Associated Universities through a contract with NASA.

R. J. A. was supported by Gemini-CONICYT grant number 32120009.

Facilities: *WISE*, *Spitzer* (IRAC), *Herschel* (PACS, SPIRE), Keck:II (NIRC2).

REFERENCES

- Agarwal, B., Khochfar, S., Johnson, J. L., et al. 2012, *MNRAS*, 425, 2854
- Ahn, C. P., Alexandroff, R., Allende Prieto, C., et al. 2013, arXiv:1307.7735
- Assef, R. J., Kochanek, C. S., Brodwin, M., et al. 2010, *ApJ*, 713, 970
- Assef, R. J., Stern, D., Kochanek, C. S., et al. 2013, *ApJ*, 772, 26
- Assef, R. J., Eisenhardt, P. R. M., Stern, D., et al. 2015, *ApJ*, in press, [arXiv:1408.1092]
- Bachetti, M., Harrison, F. A., Walton, D. J., et al. 2014, *Nature*, 514, 202
- Bardeen, J. M., Carter, B., & Hawking, S. W. 1973, *Communications in Mathematical Physics*, 31, 161
- Barth, A. J., Martini, P., Nelson, C. H., & Ho, L. C. 2003, *ApJ*, 594, L95
- Barvainis, R. 1987, *ApJ*, 320, 537
- Beck, S. C., Turner, J. L., & Gorjian, V. 2001, *AJ*, 122, 1365
- Begelman, M. C., & Rees, M. J. 1978, *MNRAS*, 185, 847
- Begelman, M. C. 2002, *ApJ*, 568, L97
- Begelman, M. C., Rossi, E. M., & Armitage, P. J. 2008, *MNRAS*, 387, 1649
- Blain, A. W., Assef, R., Stern, D., et al. 2013, *ApJ*, 778, 113
- Blain, A., et al., in preparation
- Bolton, A. S., Burles, S., Schlegel, D. J., Eisenstein, D. J., & Brinkmann, J. 2004, *AJ*, 127, 1860
- Bolton, A. S., Burles, S., Koopmans, L. V. E., Treu, T., & Moustakas, L. A. 2006, *ApJ*, 638, 703
- Bromm, V., Yoshida, N., Hernquist, L., & McKee, C. F. 2009, *Nature*, 459, 49
- Bridge, C. R., Blain, A., Borys, C. J. K., et al. 2013, *ApJ*, 769, 91
- Petty, S., et al. in preparation
- Carrasco, E. R., Gomez, P. L., Verdugo, T., et al. 2010, *ApJ*, 715, L160
- Casey, C. M., Berta, S., Béthermin, M., et al. 2012, *ApJ*, 761, 139
- Casey, C. M., Berta, S., Béthermin, M., et al. 2012, *ApJ*, 761, 140
- Couchman, H. M. P., & Rees, M. J. 1986, *MNRAS*, 221, 53
- Croom, S. M., Smith, R. J., Boyle, B. J., et al. 2004, *MNRAS*, 349, 1397
- Croom, S. M., Richards, G. T., Shanks, T., et al. 2009, *MNRAS*, 392, 19
- Cutri, R. M., Huchra, J. P., Low, F. J., Brown, R. L., & Vanden Bout, P. A. 1994, *ApJ*, 424, L65
- Cutri, R. M., Wright, E. L., Conrow, T., et al. 2012, Explanatory Supplement to the WISE All-Sky Data Release Products, 1
- Cutri, R. M., Wright, E. L., Conrow, T., et al. 2013, Explanatory Supplement to the AllWISE Data Release Products, 1
- Dey, A., Soifer, B. T., Desai, V., et al. 2008, *ApJ*, 677, 943
- Eales, S., Dunne, L., Clements, D., et al. 2010, *PASP*, 122, 499
- Eisenhardt, P. R., Armus, L., Hogg, D. W., et al. 1996, *ApJ*, 461, 72
- Eisenhardt, P. R. M., et al., in preparation
- Eisenhardt, P. R. M., Wu, J., Tsai, C.-W., et al. 2012, *ApJ*, 755, 173
- Faber, S. M., & Gallagher, J. S. 1979, *ARA&A*, 17, 135
- Fan, X., Narayanan, V. K., Lupton, R. H., et al. 2001, *AJ*, 122, 2833
- Fanidakis, N., Baugh, C. M., Benson, A. J., et al. 2012, *MNRAS*, 419, 2797
- Figer, D. F., Kim, S. S., Morris, M., Serabyn, E., Rich, R. M., & McLean, I. S. 1999, *ApJ*, 525, 750
- Figer, D. F., Najjarro, F., Gilmore, D., et al. 2002, *ApJ*, 581, 258
- Frayser, D. T., Ivison, R. J., Scoville, N. Z., et al. 1998, *ApJ*, 506, L7
- Gilli, R., Comastri, A., & Hasinger, G. 2007, *A&A*, 463, 79
- Griffin, M. J., Abergel, A., Abreu, A., et al. 2010, *A&A*, 518, L3
- Griffith, R. L., Kirkpatrick, J. D., Eisenhardt, P. R. M., et al. 2012, *AJ*, 144, 148
- Hambly, N. C., Irwin, M. J., & MacGillivray, H. T. 2001, *MNRAS*, 326, 1295
- Hewett, P. C., & Wild, V. 2010, *MNRAS*, 405, 2302
- Hirano, S., Hosokawa, T., Yoshida, N., et al. 2014, *ApJ*, 781, 60
- Hopkins, P. F., Hernquist, L., Cox, T. J., et al. 2006a, *ApJS*, 163, 1
- Hopkins, P. F., Narayan, R., & Hernquist, L. 2006b, *ApJ*, 643, 641
- Hopkins, P. F., Hernquist, L., Cox, T. J., & Kereš, D. 2008, *ApJS*, 175, 356
- Hosokawa, T., Yorke, H. W., Inayoshi, K., Omukai, K., & Yoshida, N. 2013, *ApJ*, 778, 178
- Iovino, A., Clowes, R., & Shaver, P. 1996, *A&AS*, 119, 265
- Irwin, M. J., Ibata, R. A., Lewis, G. F., & Totten, E. J. 1998, *ApJ*, 505, 529
- Johnson, J. L., Whalen, D. J., Li, H., & Holz, D. E. 2013, *ApJ*, 771, 116
- Jones, S. F., Blain, A. W., Stern, D., et al. 2014, *MNRAS*, 443, 146
- Kelly, B. C., Vestergaard, M., Fan, X., et al. 2010, *ApJ*, 719, 1315
- Kelly, B. C., & Shen, Y. 2013, *ApJ*, 764, 45
- King, A. R., & Pringle, J. E. 2006, *MNRAS*, 373, L90
- King, A. R., Pringle, J. E., & Hofmann, J. A. 2008, *MNRAS*, 385, 1621
- Lawrence, C. R., Neugebauer, G., Weir, N., Matthews, K., & Patnaik, A. R. 1992, *MNRAS*, 259, 5P
- Lawrence, A., Warren, S. J., Almaini, O., et al. 2007, *MNRAS*, 379, 1599
- Leitherer, C., Ortiz Otálvaro, P. A., Bresolin, F., et al. 2010, *ApJS*, 189, 309
- Lonsdale, C. J., Lacy, M., Kimball, A. E., et al. 2015, *ApJ*, submitted
- Lu, L., Sargent, W. L. W., Barlow, T. A., Churchill, C. W., & Vogt, S. S. 1996, *ApJS*, 107, 475
- Massaro, E., Giommi, P., Leto, C., et al. 2009, *A&A*, 495, 691
- Martin, D. C., Fanson, J., Schiminovich, D., et al. 2005, *ApJ*, 619, L1
- McConnell, N. J., Ma, C.-P., Gebhardt, K., et al. 2011, *Nature*, 480, 215
- Meisenheimer, K., & Roeser, H.-J. 1983, *A&AS*, 51, 41
- Melbourne, J., Soifer, B. T., Desai, V., et al. 2012, *AJ*, 143, 125
- Michałowski, M., Hjorth, J., & Watson, D. 2010, *A&A*, 514, A67
- Monet, D. G., Levine, S. E., Canzian, B., et al. 2003, *AJ*, 125, 984
- Mortlock, D. J., Warren, S. J., Venemans, B. P., et al. 2011, *Nature*, 474, 616
- Moustakas, L. A., Marshall, P., Newman, J. A., et al. 2007, *ApJ*, 660, L31
- Moustakas, L. A., et al. in preparation.
- Murakami, H., Baba, H., Barthel, P., et al. 2007, *PASJ*, 59, 369
- Napolitano, N. R., Capaccioli, M., Romanowsky, A. J., et al. 2005, *MNRAS*, 357, 691
- Neugebauer, G., Habing, H. J., van Duinen, R., et al. 1984, *ApJ*, 278, L1
- Ohsuga, K., & Mineshige, S. 2007, *ApJ*, 670, 1283
- Osmer, P. S., Porter, A. C., & Green, R. F. 1994, *ApJ*, 436, 678
- Pâris, I., Petitjean, P., Aubourg, É., et al. 2012, *A&A*, 548, A66
- Patnaik, A. R., Browne, I. W. A., Walsh, D., Chaffee, F. H., & Foltz, C. B. 1992, *MNRAS*, 259, 1P
- Petty, S., et al. in preparation
- Plavchan, P., Jura, M., Kirkpatrick, J. D., Cutri, R. M., & Gallagher, S. C. 2008, *ApJS*, 175, 191
- Poglitsch, A., Waelkens, C., Geis, N., et al. 2010, *A&A*, 518, L2
- Polletta, M. d. C., Wilkes, B. J., Siana, B., et al. 2006, *ApJ*, 642, 673
- Polletta, M., Tager, M., Maraschi, L., et al. 2007, *ApJ*, 663, 81
- Pope, A., Bussmann, R. S., Dey, A., et al. 2008, *ApJ*, 689, 127
- Regan, J. A., & Haehnelt, M. G. 2009, *MNRAS*, 396, 343
- Ross, N. P., McGreer, I. D., White, M., et al. 2013, *ApJ*, 773, 14
- Rowan-Robinson, M. 2000, *MNRAS*, 316, 885
- Salpeter, E. E. 1955, *ApJ*, 121, 161
- Salpeter, E. E. 1964, *ApJ*, 140, 796
- Sanders, D. B., Soifer, B. T., Elias, J. H., et al. 1988, *ApJ*, 325, 74
- Sanders, D. B., & Mirabel, I. F. 1996, *ARA&A*, 34, 749
- Schneider, D. P., Richards, G. T., Hall, P. B., et al. 2010, *AJ*, 139, 2360
- Schmidt, M. 1963, *Nature*, 197, 1040
- Shapley, A. E., Steidel, C. C., Erb, D. K., et al. 2005, *ApJ*, 626, 698
- Shapiro, S. L. 2005, *ApJ*, 620, 59

- Silk, J., & Rees, M. J. 1998, *A&A*, 331, L1
- Skrutskie, M. F., Cutri, R. M., Stiening, R., et al. 2006, *AJ*, 131, 1163
- Springel, V., Di Matteo, T., & Hernquist, L. 2005, *MNRAS*, 361, 776
- Steinhardt, C. L., & Elvis, M. 2010, *MNRAS*, 402, 2637
- Stern, D., Tozzi, P., Stanford, S. A., et al. 2002, *AJ*, 123, 2223
- Stern, D., Assef, R. J., Benford, D. J., et al. 2012, *ApJ*, 753, 30
- Stern, D., Lansbury, G. B., Assef, R. J., et al. 2014, *ApJ*, 794, 102
- Stern, D., et al. in preparation
- Subramanian, K., & Cowling, S. A. 1986, *MNRAS*, 219, 333
- Swinbank, A. M., Simpson, J. M., Smail, I., et al. 2014, *MNRAS*, 438, 1267
- Thorne, K. S. 1974, *ApJ*, 191, 507
- Tsai, C.-W., et al. in preparation
- Urry, C. M., & Padovani, P. 1995, *PASP*, 107, 803
- van Dam, M. A., Bouchez, A. H., Le Mignant, D., et al. 2006, *PASP*, 118, 310
- Véron-Cetty, M.-P., & Véron, P. 2010, *A&A*, 518, A10
- Vigotti, M., Vettolani, G., Merighi, R., Lahulla, J. F., & Pedani, M. 1997, *A&AS*, 123, 219
- Volonteri, M., & Rees, M. J. 2006, *ApJ*, 650, 669
- Volonteri, M. 2010, *A&A Rev.*, 18, 279
- Weedman, D., Sargsyan, L., Leboutteiller, V., Houck, J., & Barry, D. 2012, *ApJ*, 761, 184
- Willott, C. J., Delfosse, X., Forveille, T., Delorme, P., & Gwyn, S. D. J. 2005, *ApJ*, 633, 630
- Wilson, J. C., Miller, N. A., Gizis, J. E., et al. 2003, *Brown Dwarfs*, 211, 197
- Wise, J. H., Turk, M. J., & Abel, T. 2008, *ApJ*, 682, 745
- Wizinowich, P. L., Le Mignant, D., Bouchez, A. H., et al. 2006, *PASP*, 118, 297
- Wright, E. L., Eisenhardt, P. R. M., Mainzer, A. K., et al. 2010, *AJ*, 140, 1868
- Wu, J., Tsai, C.-W., Sayers, J., et al. 2012, *ApJ*, 756, 96
- Wu, J., Busmann, R. S., Tsai, C.-W., et al. 2014, *ApJ*, 793, 8
- Wu, X.-B., Wang, F., Fan, X., et al. 2015, *Nature*, 518, 512
- Zhang, W., Woosley, S. E., & Heger, A. 2008, *ApJ*, 679, 639
- Yu, Q., & Tremaine, S. 2002, *MNRAS*, 335, 965